Masters Theses   Dissertations and Theses

2014

Impedance Measurement of Small Antennas Over a Ground Plane Without Direct Cable Attachment

Yutong Yang
University of Massachusetts Amherst

IMPEDANCE MEASUREMENT OF SMALL ANTENNAS OVER A GROUND PLANE WITHOUT DIRECT CABLE ATTACHMENT

A Thesis Presented

by

YUTONG YANG

IMPEDANCE MEASUREMENT OF SMALL ANTENNAS OVER A GROUND PLANE WITHOUT DIRECT CABLE ATTACHMENT

A Thesis Presented

by

YUTONG YANG

Approved as to style and content by:

_____

Do-Hoon Kwon, Chair

_____

Robert W. Jackson, Member

_____

David M. Pozar, Member

_____

Christopher V. Hollot, Department Head
Department of Electrical and Computer Engineering

To my parents.

ACKNOWLEDGMENTS

I have to start my acknowledgments with my advisor Prof. Do-Hoon Kwon. I am grateful to him for his technical advice, patience, encouragement, and support during my thesis research.

I would like to thank my group members, Adebayo Adeyemi, Hsieh-Chi Chang, Caglar Emiroglu, and Amin Nikravan, for their help in my research.

Furthermore, I would like to thank my friends at University of Electronic Science and Technology of China, for their supports and treating me like family when we first learned the courses on Microwave Engineering together.

Thanks are extended to my friends especially Wei Li, Chuan Zhang, Teer Gele and Keqiang Wu for their encouragement in study and help on my living in Amherst.

Last but not the least, I want to thank my father Xiangdong Yang and my mother Jiarui Yang. I am so grateful to you for the constant support, understanding and love. I would especially thank my father, for the great suggestion to help me overcome a difficulty on my thesis research.

ABSTRACT

IMPEDANCE MEASUREMENT OF SMALL ANTENNAS OVER A GROUND PLANE WITHOUT DIRECT CABLE ATTACHMENT

YUTONG YANG

B.Sc., UNIVERSITY OF ELECTRONIC SCIENCE AND TECHNOLOGY OF

CHINA

M.S.E.C.E., UNIVERSITY OF MASSACHUSETTS AMHERST

Directed by: Professor Do-Hoon Kwon

An indirect impedance measurement approach that does not require direct cable attachment or large space using a two-port network is presented. Using a straight wire monopole as an interrogating antenna and measured impedances of three calibration standards, the input impedance of a small spherical helix dipole over a ground plane is retrieved. It is found that accurate result is obtained around the dipole resonance frequency. The accuracy and sources of error are discussed.

TABLE OF CONTENTS

LIST OF TABLES

LIST OF FIGURES

CHAPTER 1

INTRODUCTION

For electrically small antennas, cable attachment for direct impedance measurement can lead to inaccurate and unreliable results because it changes the antenna's structure and current distribution [1]. Only for antennas having structural symmetry and excited in the symmetry plane, a half of the antenna can be mounted on a ground plane and direct cable excitation can be applied through the ground plane to get accurate measurement results.

There are indirect measurement approaches for the impedance and/or the radiation pattern of an antenna without direct cable attachment. Backscattering radar cross sections (RCS) of an antenna under test (AUT) using three different loads at the antenna port can be measured to retrieve the impedance and pattern [2]. This far-zone scattering technique has been extended to multiport antenna characterizations [3], where polarimetric RCS measurements are utilized. Based on the theory of loaded scatterers [4], the RCS-based method can be cast in a multi-port network formulation, where the AUT's impedance is the self-impedance of the antenna port. The AUT impedance may be obtained starting with a standard two-port network formulation. Like in the RCS approach, three separate measurements with different loads at the AUT terminal are needed. The impedance retrieval expression also applies to the RCS measurement approach if scattering parameters are appropriately defined in terms of complex RCS values [5]. In [6], two-port measurement results using different probe antennas and AUTs in the far zone of each other were reported.

In this study, a two-port network approach is investigated for the impedance measurement of an electrically small antenna. Specifically, a measurement is designed, simulated, and performed for a vertically polarized spherical helix antenna over a ground plane at 300 MHz [7]. Since the radiation pattern of an electrically small antenna is essentially that of a short dipole antenna, the primary interest is accurate measurement of the antenna impedance. Hence, no far-zone measurement requiring a large space is necessary. It is found that the two-port network approach allows an accurate impedance measurement even when the two antennas are separated within a wavelength.

For comparison, the input impedance has also been measured using several direct excitation approaches.

CHAPTER 2

INDIRECT MEASUREMENT TECHNIQUES

There are several techniques for impedance measurement of an antenna that can avoid direct cable attachment for excitation. This chapter is to further explain these techniques.

2.1 Determination of Antenna Impedance By RCS Measurement
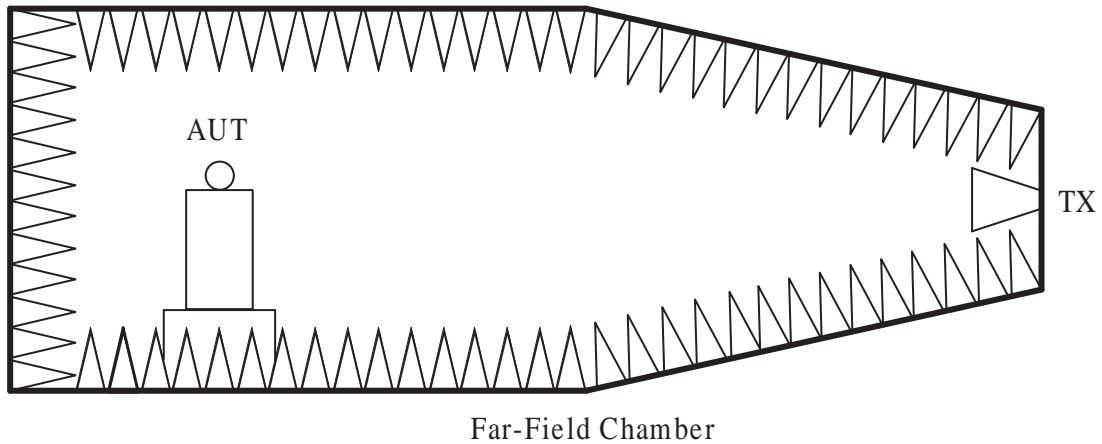
Figure 2.1. Setup for RCS measurement approach.

Figure 2.1 illustrates an impedance measurement setup by RCS measurement. A transmit/receive antenna and the AUT form a two-port network. The incident power wave vector [**a**] and the output power wave vector [**b**] have following relation:

$$
\begin{bmatrix} b_1 \\ b_2 \end{bmatrix} = \begin{bmatrix} S_{11} & S_{12} \\ S_{21} & S_{22} \end{bmatrix} \begin{bmatrix} a_1 \\ a_2 \end{bmatrix},
\tag{2.1}
$$

where the subscript 1 denotes the port of the transmit antenna, and the subscript 2 denotes the port of the AUT. In [3], the two-port scattering matrix is extended into a multiport matrix.

Assuming the structural scattering is negligible, let $\mathbf{E}^i$ and $\mathbf{E}^s$ denote the electric fields of the incident plane wave and the scattered spherical wave, respectively. The RCS σ is defined as [8]

$$\sigma = |S_{11}|^2 = \lim_{r\to\infty} 4\pi r^2 \frac{|\hat{e}^i \cdot \mathbf{E}^s|^2}{|\mathbf{E}^i|^2}, \tag{2.2}$$

where $\hat{e}^i$ is the polarization unit vector of the incident field. One can take a square root of (2.2) and restore the phase information of the scattered field. The input reflection coefficient of the excitation port can be defined to be [5]

$$\Gamma_1 = \frac{\sqrt{\sigma}}{2\sqrt{\pi}} = \lim_{r\to\infty} r \frac{\hat{e}^i \cdot \mathbf{E}^s}{\hat{e}^i \cdot \mathbf{E}^i}. \tag{2.3}$$

The magnitude as well as the phase of the input reflection coefficient at port 1 can be found using (2.3).

For the two-port network formed by the transmit antenna (port 1) and the AUT (port 2),

$$\Gamma_2 = \frac{b_2}{a_2} = S_{22} + \frac{S_{12}S_{21}\Gamma_1}{1 - S_{11}\Gamma_1} \tag{2.4}$$

where the S parameters are for the two-port network, Γ_1 and Γ_2 denote the reflection coefficients at port 1 and port 2 respectively. In order to retrieve Γ_2 in (2.4), three different loads attached to the port of AUT are required, hence three different Γ_1 can be obtained by measuring the scattered field $\mathbf{E}^s$ and using (2.3). Substituting these Γ_1 into (2.4) and eliminating the S parameters, Γ_2 can be retrieved. The associated input impedance Z_2 at port 2 that is sought can be obtained from Γ_2. This technique requires that the TX antenna and AUT are in the far field of each other, as illustrated in Figure 2.1.

4

2.2 Graphical Method Using Scattering Cross-Section Measurement
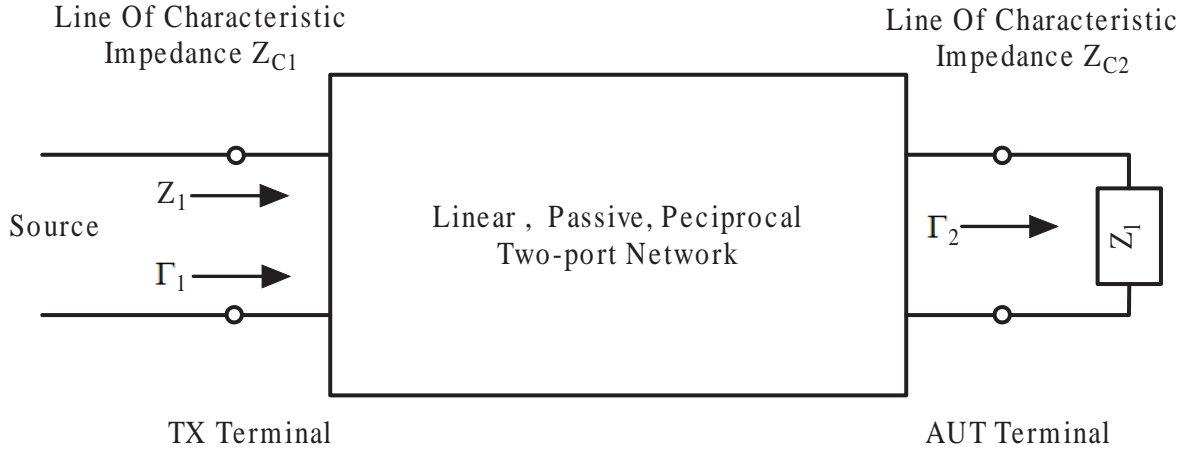
Figure 2.2. Block diagram of two-port network [2].

In [2], a graphical approach for finding the impedance of AUT using the Smith chart has been presented. The AUT and transmit/receive antenna form a linear reciprocal two-port network (Figure 2.2). The reflection coefficient at port 1 is proportional to the signal scattered from the AUT, hence knowing the scattering cross-section is essentially the same as knowing the amplitude of the input reflection coefficient.

A modified load-reflection coefficient at port 2 is defined to be [2]

$$\Gamma_m = \frac{Z_l - Z_a^*}{Z_l + Z_a},\tag{2.5}$$

where Z_l is the load impedance at port 2. If coupling between two ports is negligible, $Z_a = R_a + jX_a$ is the impedance of the AUT that we seek. According to [9], Γ_1 is linearly related to Γ_m:

$$\Gamma_1/B = C + \Gamma_m,\tag{2.6}$$

where B and C are constants. From (2.6), Γ_1 can be located on the Γ_m-plane Smith chart using a vector diagram; it can also be found from (2.6) that the maximum and

minimum scattering cross-sections of Γ_1 with loss-free loads that correspond to Γ_m given by

$$|\Gamma_1^{max}|^2 = |B|^2(|C| + 1)^2$$
$$|\Gamma_1^{min}|^2 = |B|^2(|C| - 1)^2$$

(2.7)

lie on the two end points of a diameter of the Γ_m-plane Smith chart. Similarly, the arithmetic average of the maximum and minimum scattering cross-sections of Γ_1 with loss-free loads that correspond to Γ_m given by

$$|\Gamma_1^{av1}|^2 = |B|^2(|C|^2 + 1)$$
$$|\Gamma_1^{av2}|^2 = |B|^2(|C|^2 + 1)$$

(2.8)

also lie on the two end points of another diameter of the Γ_m-plane Smith chart. Figure 2.3 shows these four complex values Γ_m^{max}, Γ_m^{min}, Γ_m^{av1} and Γ_m^{av2} on the Γ_m-plane Smith chart, where $\overrightarrow{SO}$, $\overrightarrow{OT}$ and $\overrightarrow{ST}$ are C, Γ_m and Γ_1/B in (2.6), respectively. It can be seen that these four complex values—Γ_m^{max}, Γ_m^{min}, Γ_m^{av1} and Γ_m^{av2}—are disposed $90°$ from one another in the Γ_m-plane.

Figure 2.4 shows how to determine Z_a using a Smith chart. Let the loads on the AUT be loss-free, such that the four points, Γ_2^{max}, Γ_2^{min}, Γ_2^{av1} and Γ_2^{av2}, can be plotted on the rim of the Smith chart. According to [10], these four points are associated with their counterparts Γ_m^{max}, Γ_m^{min}, Γ_m^{av1} and Γ_m^{av2} by an inversion construction. Choose two arbitrarily points U and V located on the rim of the Γ_2-plane Smith chart that subtend $90°$ at the center of the chart. Given any two experimental points, say Γ_2^{max} and Γ_2^{av1}, the lines joining U and V with Γ_2^{max} and Γ_2^{av1} will intersect at one point W. The three points W, Γ_2^{max} and Γ_2^{av1} define a circle. A similar procedure defines another circle with Γ_2^{min} and Γ_2^{av1} used together with the point intersected by the lines joining U and V with Γ_2^{min} and Γ_2^{av1} instead. The intersection point of the two circles is the impedance of the AUT.
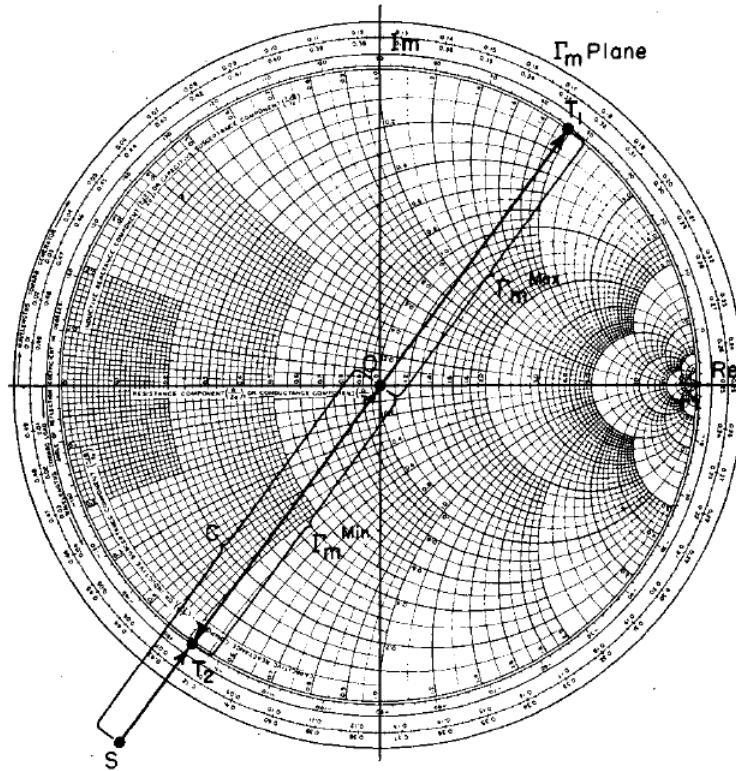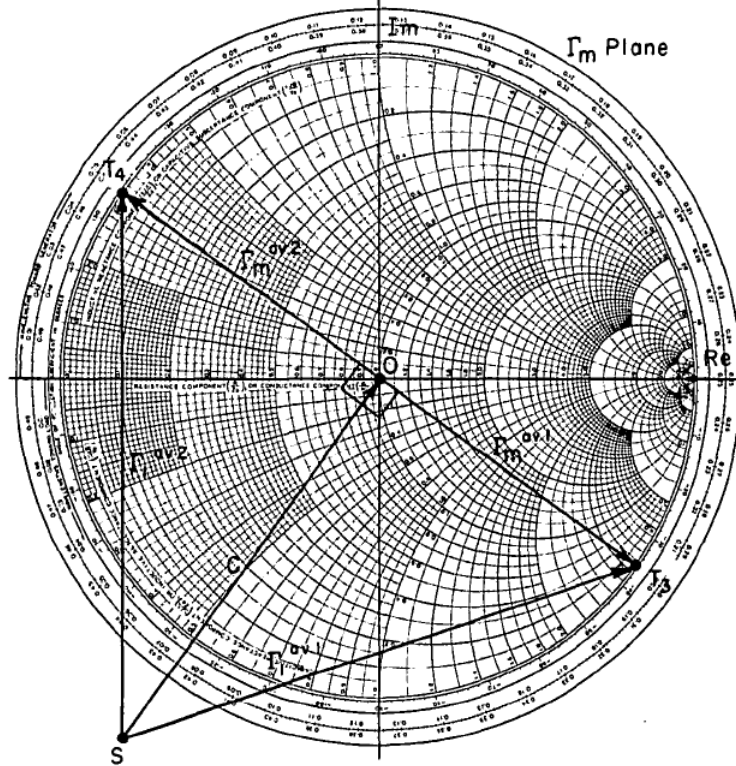
Figure 2.3. Vector diagram under special conditions of scattering cross-sections of Γ_1 [2]. (a) Maximum and minimum cross-section. (b) Average cross-section.
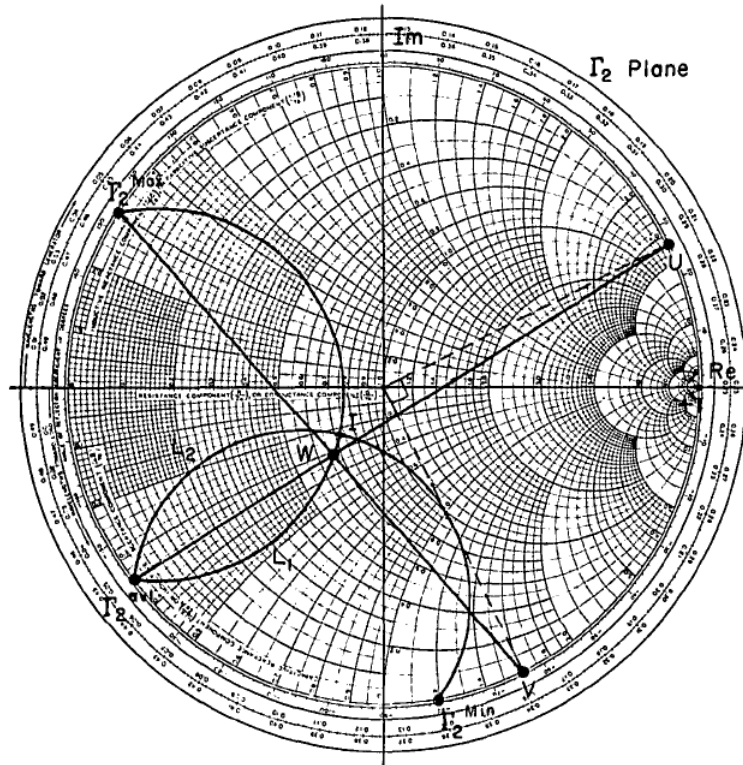
Figure 2.4. Determination of Z_a from intersection of two circles [2].

This graphical approach requires three measurements, with different loads making Γ_2 to be Γ_2^{max}, Γ_2^{min}, Γ_2^{av1} or Γ_2^{av2}. Only three out of four Γ_2 values are needed. Since the reflection coefficient at port 1 is proportional to the signal scattered from the AUT, this approach is based on the same idea as the RCS approach in Chapter 2.1, which requires a far-field measurement setup, but provides an easier and faster solution on a Smith chart.

CHAPTER 3

INDIRECT MEASUREMENT USING TWO-PORT NETWORK
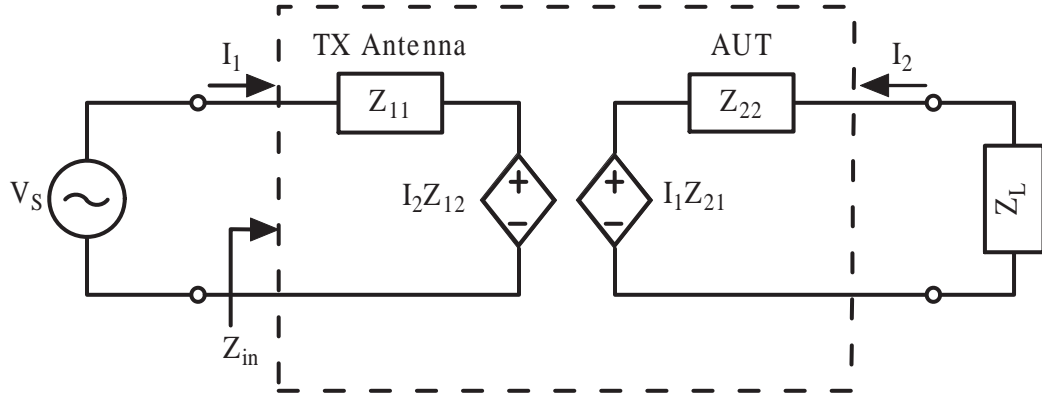
Figure 3.1. Two-port network formed by a TX antenna and an AUT.

A transmitting (TX) antenna and an AUT form a two-port network (Figure 3.1). Assigning the TX antenna port as port 1 and the AUT port as port 2, consider a load impedance Z_L connected to port 2, the input impedance Z_{in} at port 1 is given by [11]

$$Z_{\text{in}}(\omega) = Z_{11}(\omega) - \frac{Z_{12}(\omega)Z_{21}(\omega)}{Z_{22}(\omega) + Z_L(\omega)}, \tag{3.1}$$

where Z_{11}, Z_{22} are the self impedances and Z_{12}, Z_{21} are the mutual impedances. If the separation d between the two antennas is far enough, the open-circuited TX antenna will have a negligible loading effect on the AUT, so that the input impedance of the AUT Z_{AUT} is equal to Z_{22}. The effect of d is discussed in Chapter 4.1. This effect of coupling can be eliminated by defining port 1 to be a plane-wave port in the far zone from the AUT, which is the main idea of the RCS-based method [3].

At least three known loads and corresponding Z_{in1}, Z_{in2} and Z_{in3} at the AUT port are required to eliminate Z_{11}, Z_{12} and Z_{21} in (3.1):

$$Z_{\text{in1}} = Z_{11} - \frac{Z_{12}Z_{21}}{Z_{22} + Z_{L1}}, \tag{3.2a}$$

$$Z_{\text{in2}} = Z_{11} - \frac{Z_{12}Z_{21}}{Z_{22} + Z_{L2}}, \tag{3.2b}$$

$$Z_{\text{in3}} = Z_{11} - \frac{Z_{12}Z_{21}}{Z_{22} + Z_{L3}}, \tag{3.2c}$$

$$\frac{(3.2a) - (3.2b)}{(3.2a) - (3.2c)} \Rightarrow \frac{Z_{\text{in1}} - Z_{\text{in2}}}{Z_{\text{in1}} - Z_{\text{in3}}} = \frac{(Z_{L2} - Z_{L1})(Z_{22} + Z_{L3})}{(Z_{L3} - Z_{L1})(Z_{22} + Z_{L2})}. \tag{3.3}$$

From (3.3), Z_{AUT} is found to be

$$Z_{\text{AUT}} = Z_{22} = \frac{xZ_{L2} - Z_{L3}}{1 - x},$$
$$\text{where } x = \frac{(Z_{\text{in2}} - Z_{\text{in1}})(Z_{L3} - Z_{L1})}{(Z_{\text{in3}} - Z_{\text{in1}})(Z_{L2} - Z_{L1})}. \tag{3.4}$$

In order to simplify the expression, we choose a commonly used set of load impedances: a short ($Z_{L,s} = 0$), a 50-Ω load ($Z_{L,l} = 50$) and an open ($Z_{L,o} = \infty$). Substituting Z_{L1}, Z_{L2} and Z_{L3} with these loads, (3.4) can be simplified as

$$Z_{\text{AUT}} = Z_{22} = -(Z_{L,l} - Z_{L,s})\frac{Z_{\text{in},o} - Z_{\text{in},l}}{Z_{\text{in},s} - Z_{\text{in},l}}. \tag{3.5}$$

This indirect technique relies on accurate measurement of Z_{in} as well as differences in Z_{in} for different AUT load impedances. Either inaccuracies in Z_{in} or negligible differences in Z_{in} among different loads will compromise the accuracy of the retrieved Z_{AUT}.

CHAPTER 4

INDIRECT MEASUREMENT OF A SPHERICAL DIPOLE ANTENNA OVER GROUND

(a)

(b)
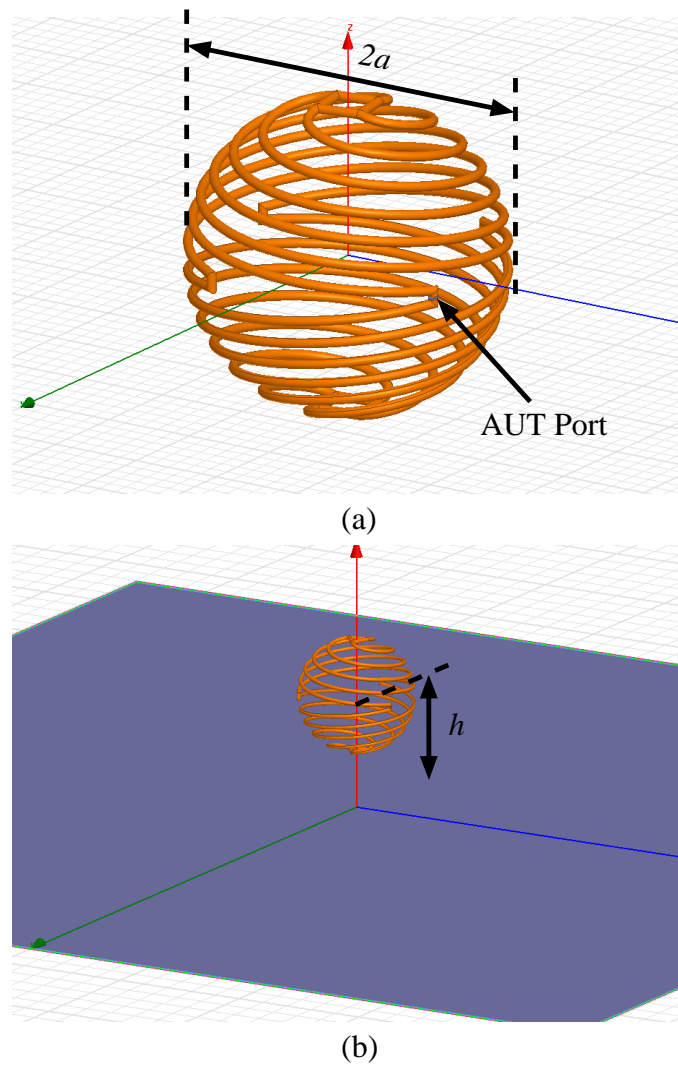
Figure 4.1. Spherical helix antenna resonance at 300 MHz. (a) In free space. (b) Over ground.

	No. of Arms	No. of Turns	ka	kh
Ant. in fs	4	1.635	0.2626	-
Ant. over gnd	3	1.5883	0.2626	0.5252

	length (cm)	$\Delta\omega_{3\text{dB}}/\omega_0(\%)$	$\Delta\omega_{10\text{dB}}/\omega_0(\%)$	Q
Ant. in fs	65.8462	2.27	0.77	107.37
Ant. over gnd	64.0788	4.30	1.43	53.10

Table 4.1. Properties of spherical helix antenna in free space and over ground.

Figure 4.1(a) shows a spherical helix dipole antenna in free space designed for $f_0 = 300$ MHz [12]. In free space, the radiation pattern of this antenna is essentially that of a short dipole antenna, and the quality factor Q of this spherical antenna agrees well with the Thal bound of Q [12] [13]. A horizontal bisecting plane serves as the symmetry plane for this antenna and the excitation point lies in the symmetry plane. Hence, a half of the antenna (a monopole version) can be fabricated, mounted on a large ground plane and directly excited at the port using a coaxial cable from below the ground plane to measure its impedance.

Figure 4.1(b) is a spherical helix antenna of the same design over a ground plane designed for $f_0 = 300$ MHz [7]. It is designed to have the same size as the free-space dipole in Figure 4.1(a). Table 4.1 summarizes the design parameters of the two spherical helix antennas in Figure 4.1, where k is the free-space wavenumber, a is the radius of the antenna, and h is the height from the center of the antenna to the ground. The design equations of the spherical helix antenna can be found in [12, Equation (1)-(5)]. For the antenna over a ground plane, the numbers of arms and the number of turns for each arm are adjusted for impedance match to 50 Ω at the AUT port. It has been predicted that this antenna over a ground plane has a broader bandwidth than the antenna of the same size in free-space, by approximately a factor of two [7], as shown in the Q factors in Table 4.1 (evaluated based on [14,

Equation (96)]) and Figure 4.2. In small antennas research, predicted and realized bandwidths for a given design space are of great interest. A predicted decrease in Q, or an enhanced bandwidth, needs experimental validation. Hence, it is essential to verify the antenna's enhanced bandwidth by measurement to support the theory. Therefore, an accurate impedance measurement is also required for the antenna in Figure 4.1(b). However, since the antenna is located above a ground plane, its excitation port is no longer on the symmetry plane. Hence, the measurement approach suitable for Figure 4.1(a) using a monopole version is no longer applicable.

The spherical helix antenna is an electrically small antenna with $ka = 0.2626 < 1$. Directly attaching an excitation cable to its port for impedance measurement may significantly perturb the current distribution and slightly enlarge the antenna in effect, which will contribute to increasing the bandwidth. The purpose for this impedance measurement is to verify the theory in [7] that the bandwidth of a small antenna can be enhanced by the introduction of a ground plane. All other factors in measurements that can potentially result in an increased bandwidth should be eliminated. The approaches described in Chapter 2 are not practical because they require far-field measurements; for the AUT in Figure 4.1(b), an unrealistically large ground plane is needed in the measurement setup, which extends from the TX antenna to the AUT. Additionally, a large anechoic chamber that operates at 300 MHz is needed. Therefore, the indirect two-port approach described in Chapter 3 is a candidate method of accurate impedance measurement while avoiding direct cable attachment, because it does not require far-field measurements as long as the separation between the two antennas is far enough to make the coupling between the AUT and the open-circuited TX antenna weak. For the AUT in Figure 4.1(b), the indirect two-port approach of Chapter 3 is used for measuring the impedance of the AUT using a thin-wire monopole antenna as the TX antenna.
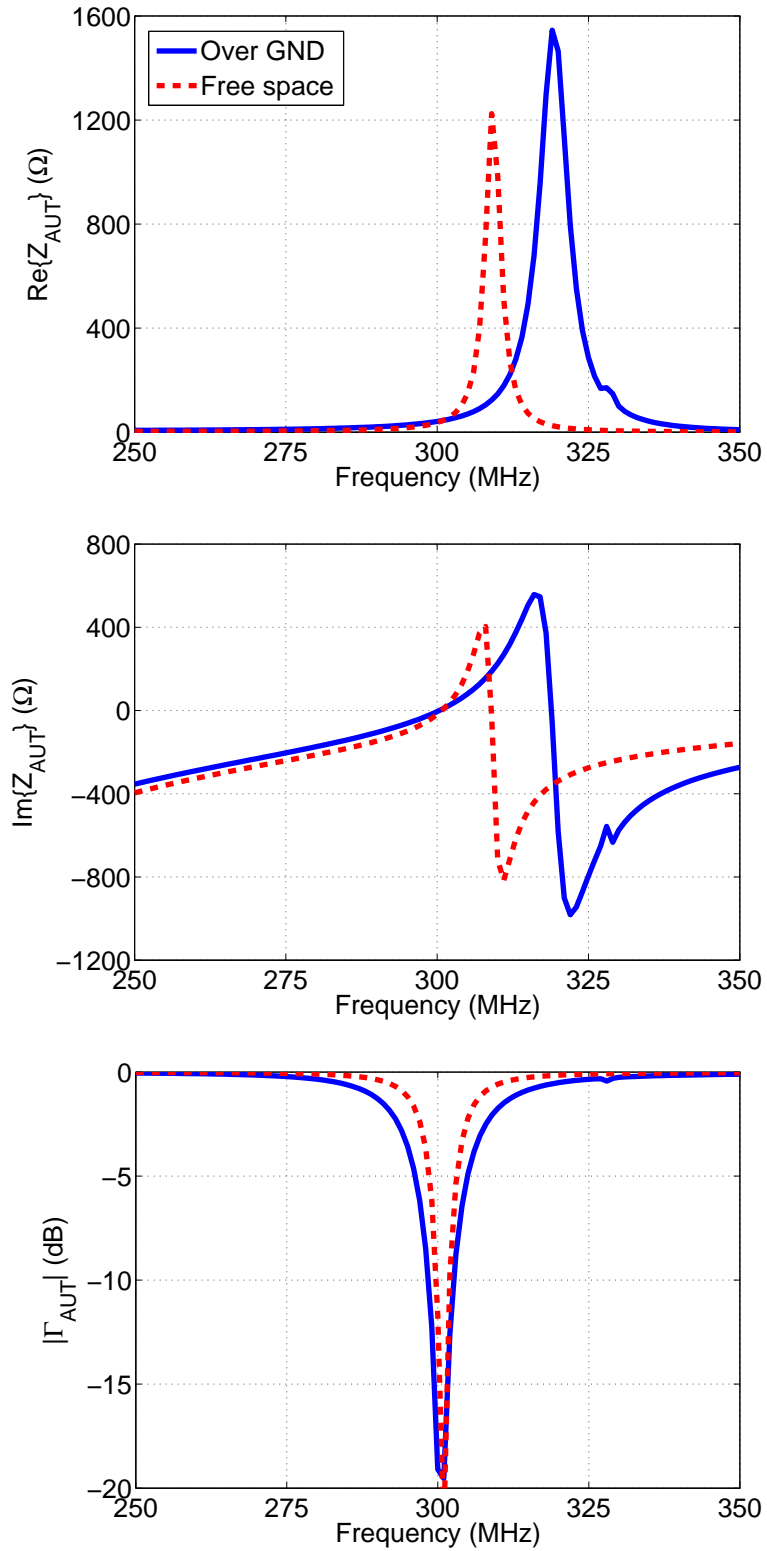
Figure 4.2. Comparison of simulated results of the spherical helix antenna over infinite GND and in free space. (a) Re$\{Z_{\text{AUT}}\}$. (b) Im$\{Z_{\text{AUT}}\}$. (c) $|\Gamma_{\text{AUT}}|$.

15

4.1   Simulation Results

(a)

(b)
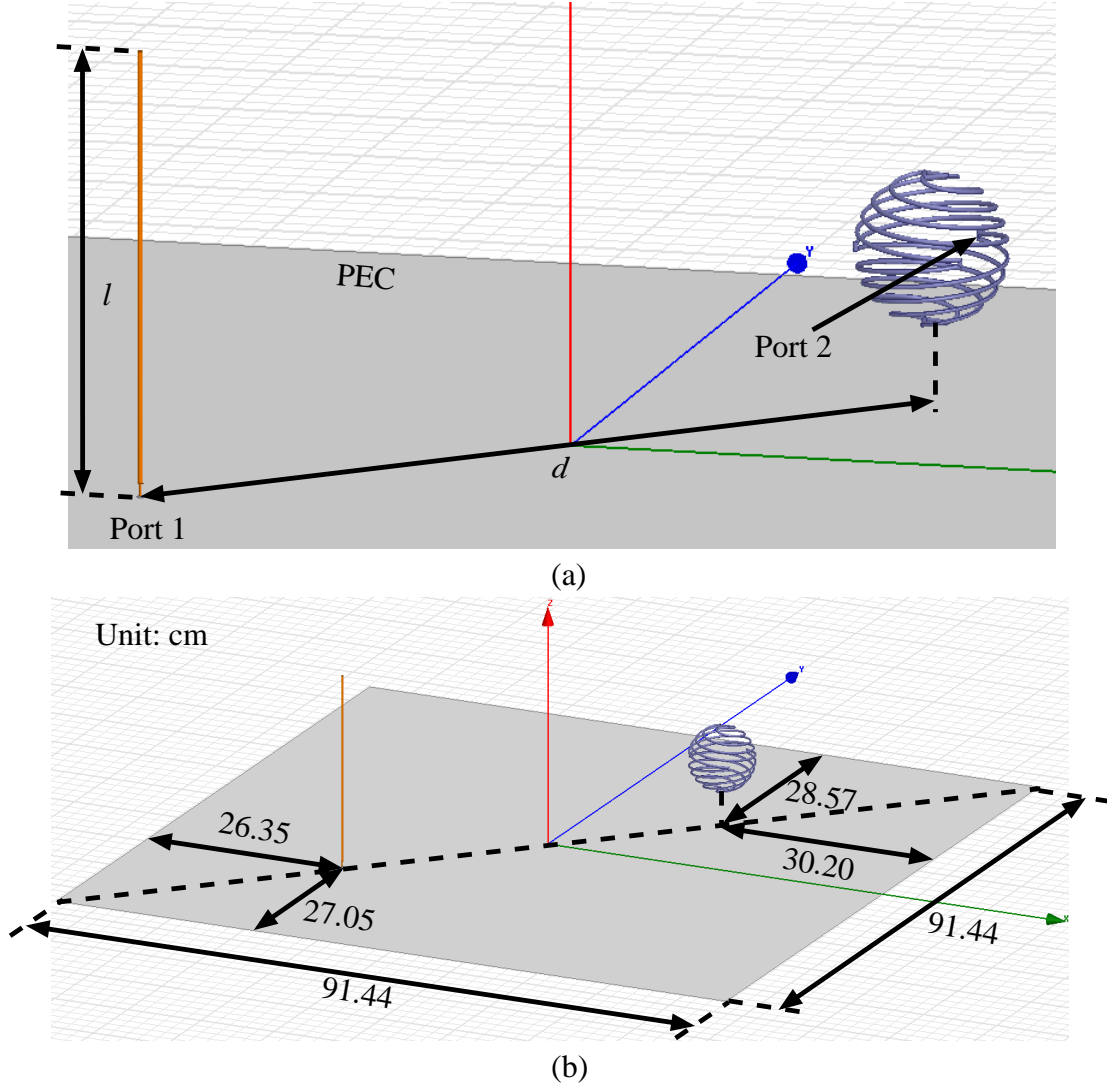
Figure 4.3. Indirect impedance measurement setup using a two-port network configuration. (a) Setup of the two-port network. (b) Dimensions of the setup.

Figure 4.3 illustrates the two-port setup. A thin-wire monopole ($l = 245.5$ mm, wire radius 1.3 mm) for resonance at $f = f_0$ is used as the TX antenna. The two antennas are $\lambda_0/2$ apart (λ_0 = free-space wavelength at $f = f_0$) for not being too close for the TX antenna's structural scattering to be strong enough to affect the results, nor too far away for the coupling to be too weak to be accurately measured. For practical purposes, the infinite ground is replaced by a finite 3'×3' ground plane

Figure 4.4. Comparison of the simulated results of a spherical helix dipole antenna over a ground plane with $kh = 0.5252$ between direct and indirect approaches. The antenna separation for indirect approach is $d = 50$ cm. (a) Z_{AUT}. (b) $|\Gamma_{\text{AUT}}|$.

	Q	$\Delta\omega_{3\text{dB}}/\omega_0(\%)$	$\Delta\omega_{10\text{dB}}/\omega_0(\%)$
Ant. over inf. gnd	53.10	4.30	1.43
Ant. over 3'×3' gnd	55.43	4.20	1.40

Table 4.2. Q factors and bandwidths of spherical helix antenna over infinite and finite ground planes using direct excitation.

of an aluminum plate. The Z-parameters of the two-port network are obtained using Ansys HFSS.

Figure 4.4 compares the simulated impedance and reflection coefficient of the AUT obtained using direct and indirect excitations with respect to frequency. A direct excitation of the AUT over an infinite ground (blue solid) shows the ideal result. In HFSS, an equivalent free-space configuration after application of the image theory was used to find the ideal input impedance; the two lumped ports were excited with the same magnitude and 180° out of phase. The impedance obtained using a directly excited AUT over a finite 3'×3' ground plane (red dash) is a measurable quantity that serves as a reference that the indirect approach (black dash-dot) needs to reproduce. Negligible differences among the three sets of impedances in Figure 4.4 indicate that the 3'×3' ground plane size has little influence on the impedance and that the indirect approach accurately retrieves Z_{AUT} and $|\Gamma_{\mathrm{AUT}}|$ over a wide bandwidth. Table 4.2 further confirms that using a finite ground plane will have a negligible influence on the bandwidth of the AUT.

Since the indirect approach relies on the assumption that structural scattering of the TX antenna is negligible ($Z_{\mathrm{AUT}} = Z_{22}$), this condition needs to be validated. Over an infinite ground, Figure 4.5 compares the direct and indirect impedance results at $f = 300$ MHz as a function of d. It is observed that Z_{AUT} of the indirect method converges to that of the direct excitation. In $d > 0.4\lambda_0$, the agreement is excellent. A reasonable agreement is obtained even with a small electrical separation around $d = 0.1\lambda_0$.

4.2   Measurement Setup

Utilizing a custom 3-D printed plastic mold with grooves, a spherical helix dipole antenna was manually fabricated out of gauge-10 (diameter = 2.6 mm) copper wire. Figure 4.6 shows a photo of the top and bottom halves of the fabricated dipole on the
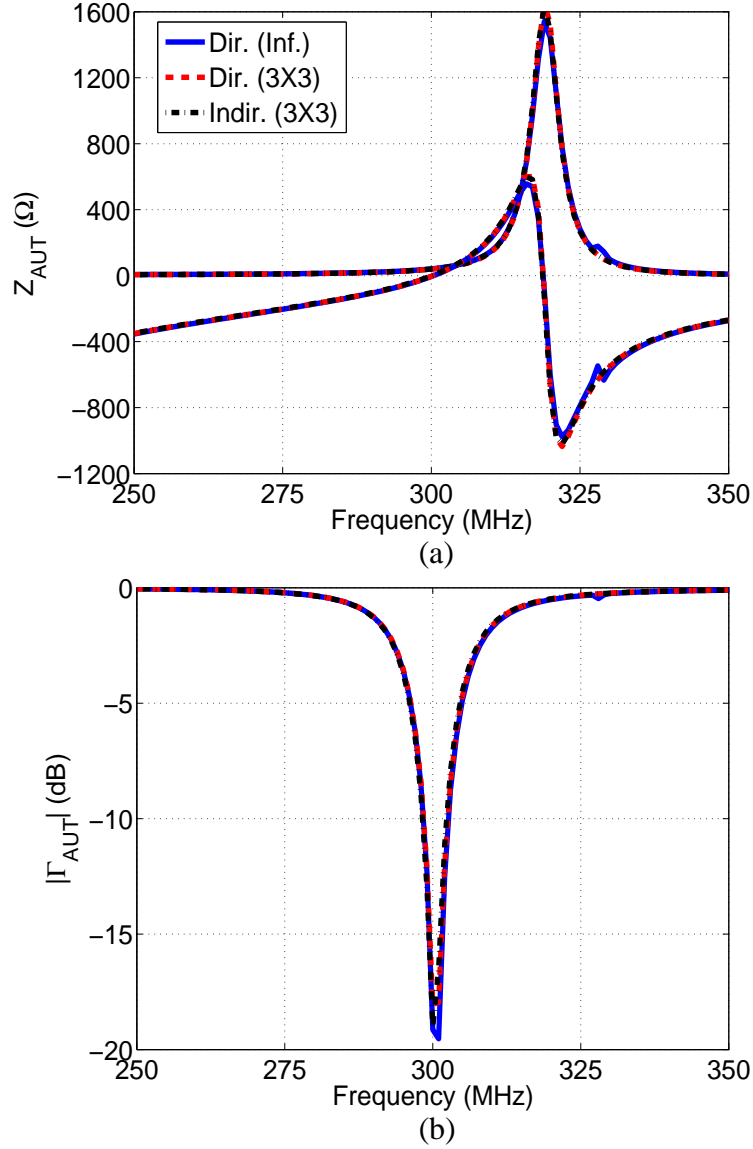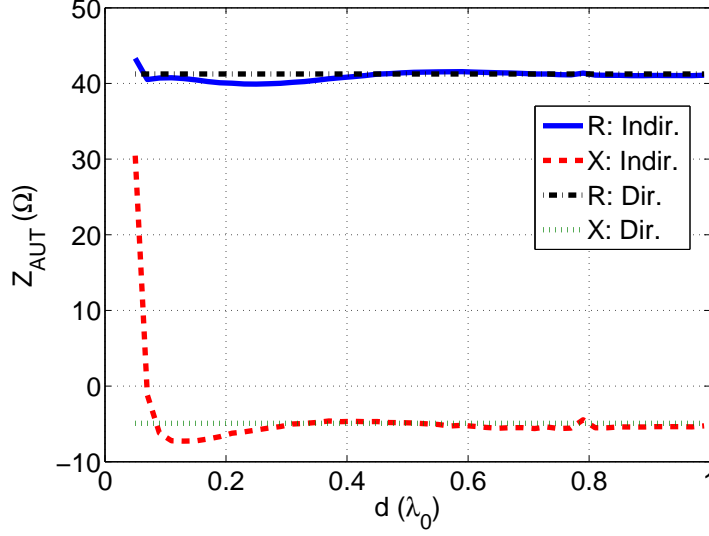
Figure 4.5. Comparison of the simulated Z_{AUT} of a spherical helix dipole antenna over a ground plane between direct and indirect approaches at $f = 300$ MHz with respect to d.

plastic mold. Measurement of Z_{in} was taken in an outdoor open space (Figure 4.7) rather than an indoor environment in order to avoid having the effect of multiple reflections in measured values. The antenna was supported by a Styrofoam block ($\epsilon_r = 1.03$) with cut grooves to stabilize the location of the spherical helix antenna, as shown in Figure 4.8. The foam block was added and simulated in the two port setup in HFSS, and results showed no difference from the ideal case of the antenna without support. A short piece of gauge-10 copper wire was used as $Z_{L,s}$, and standard 1206-sized chip resistors (49.9 Ω and 1 MΩ) were used as $Z_{L,l}$ and $Z_{L,o}$, respectively. All loads were directly soldered to the two arms of the antenna (Figure 4.8).

Using (3.5), simulated and measured input impedances and return loss values were retrieved and they are shown in Figure 4.10. The measured results (red dash) do not agree with the simulated results (blue solid), which is mainly attributed to the different soldering conditions for different loads and a slightly changed geometry of the AUT as different loads are attached. Hence, the three Z_{in} in (3.5) actually denote

the input impedance at port 1 for three different two-port network, which makes the retrieved Z_{AUT} inaccurate and unreliable.

In order to connect the loads to the AUT port in a reproducible and repeatable manner, the antenna was augmented by a male SMA connector at the AUT port. For the added connector and the physical loads not to affect the antenna characteristics noticeably, it needs to be verified that negligible current flows over the connector. The connector [Figure 4.11(c)] has been modeled and added to the port of AUT in HFSS. At the design frequency, Figure 4.11(a) compares the antenna surface current distribution between ideal (a point) and physical (connector and load volumes in proper sizes) ports when directly excited at 300 MHz. Negligible current over the SMA connector and the load confirms that adding an SMA connector will have little effect on evaluating the AUT impedance. In contrast, the augmented antenna with the connector has a resonance around 335.5 MHz that the AUT alone doesn't have, where a strong surface current is induced over the connector and load as shown in Figure 4.11(b). Fortunately, this resonance is outside the bandwidth of interest. Two torque wrenches were used to connect the loads to the SMA connector, with one applied to the nut of the connector and the other on the load such that the load can be connected correctly every time.

The load values attached to the AUT port were measured values of standard loads in a standard network-analyzer setup. We chose a set of 3.5-mm female SMA calibration standards from Fairview Microwave as load impedances: a short (SC2141) for $Z_{L,s}$, a termination (ST1825) for $Z_{L,l}$ and an open (SC2170) for $Z_{L,o}$. Figure 4.12(a) shows a photo of these calibration standards, of which the impedance can be measured easily and accurately. The dimensions of the loads are not too large to affect the surface current distribution on AUT. Figure 4.12(b) shows the measured impedances of these calibration standards on a Smith chart. They slightly deviate from the ideal values and have a small degree of frequency dependence.
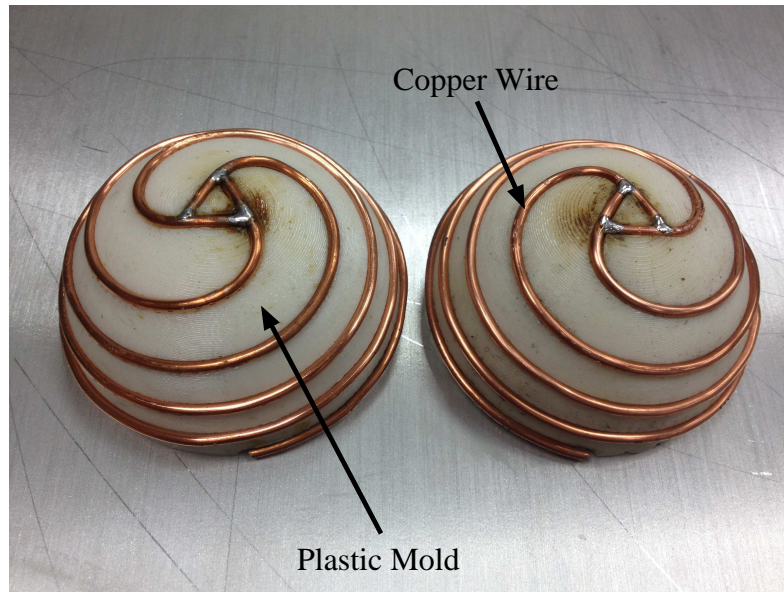
Figure 4.6. Fabricated copper wires on plastic molds.

Figure 4.7. Indirect impedance measurement environment.
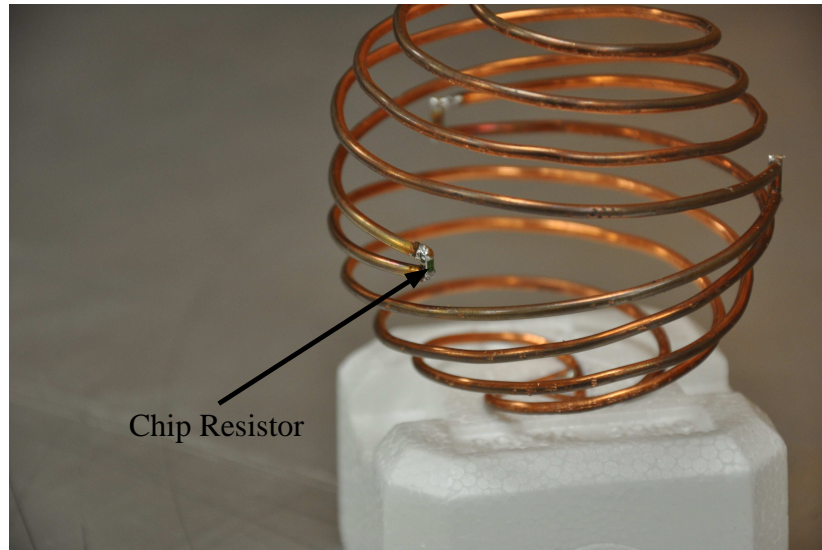
Figure 4.8. Spherical helix antenna with 1206 chip resistors.
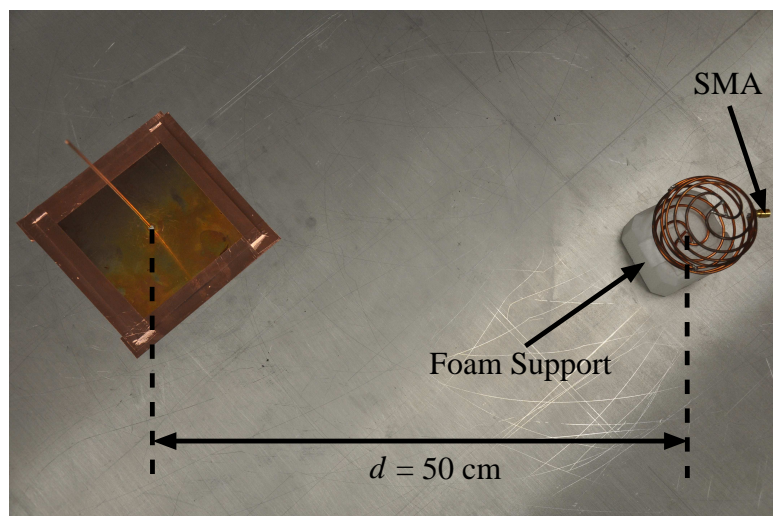
Figure 4.9. Indirect impedance measurement setup.
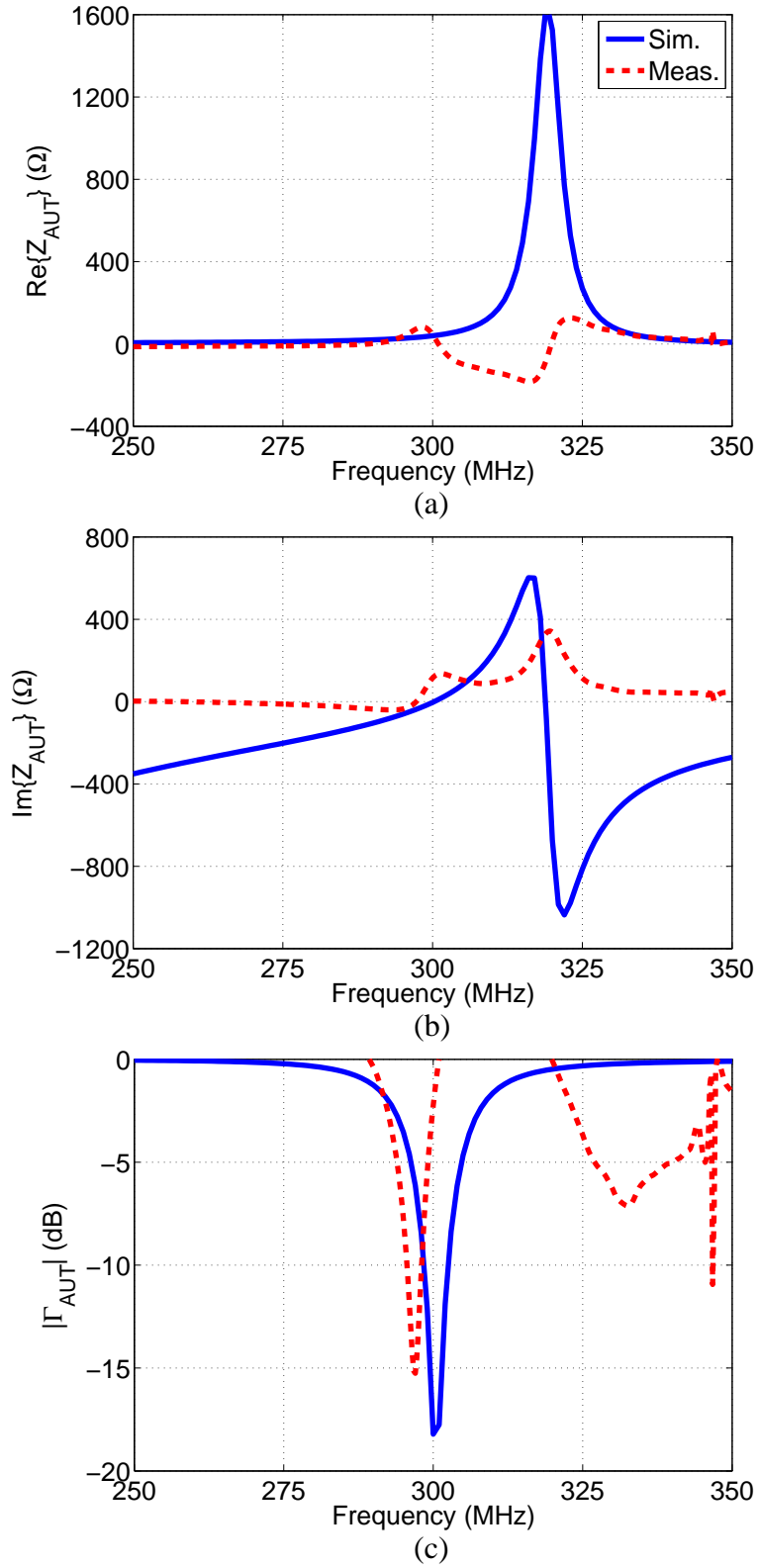
Figure 4.10. Comparison of the simulated and measured Z_{AUT} with chip resistors attached to the AUT port. (a) Re$\{Z_{\mathrm{AUT}}\}$. (b) Im$\{Z_{\mathrm{AUT}}\}$. (c) $|\Gamma_{\mathrm{AUT}}|$.

23
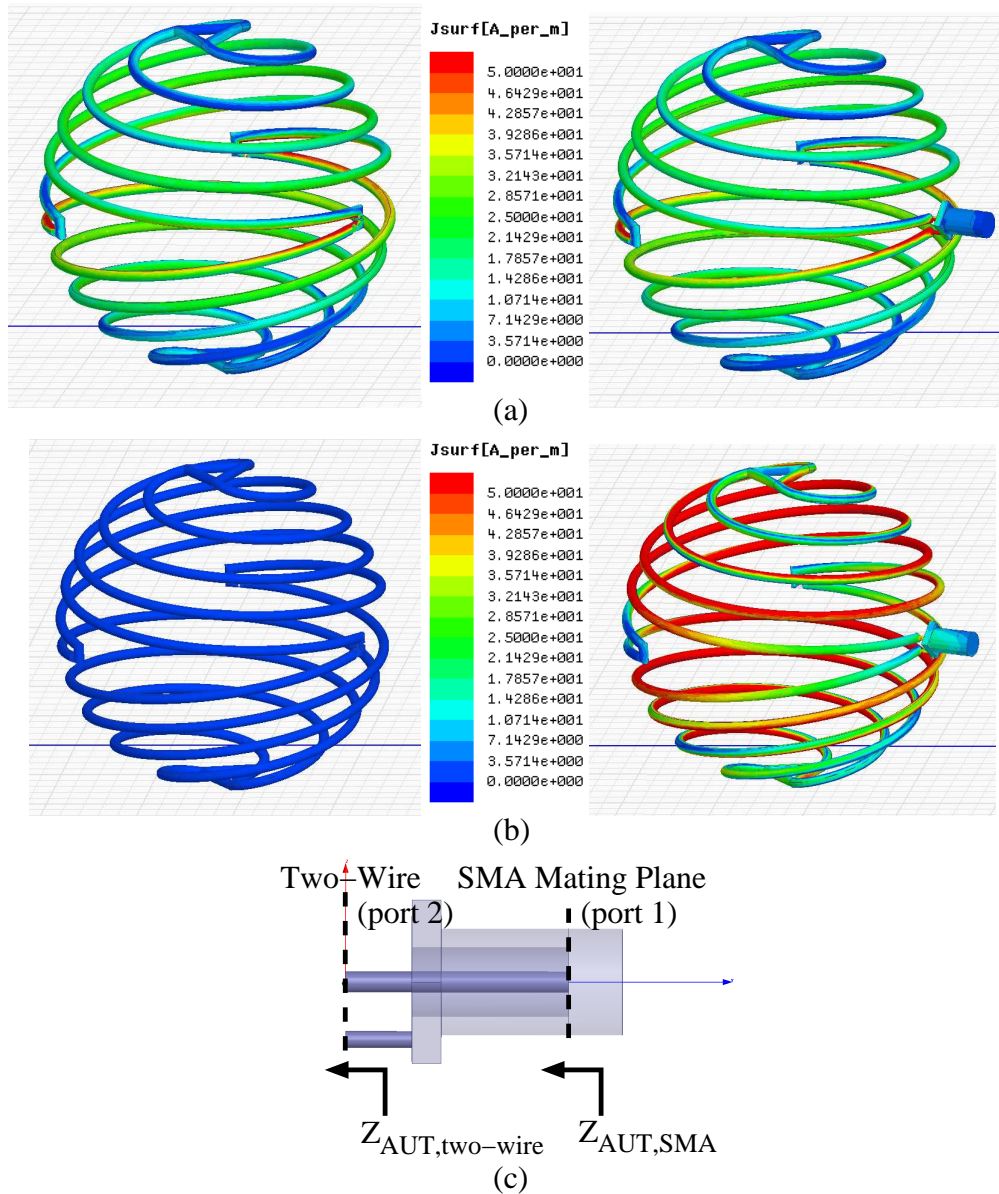
Figure 4.11. Effect of an SMA connector used for load attachment. (a) Surface current distributions at 300 MHz. The two distributions use the same color legend. (b) Surface current distributions at 335.5 MHz. The two distributions use the same color legend. (c) Model of the SMA connector in HFSS.
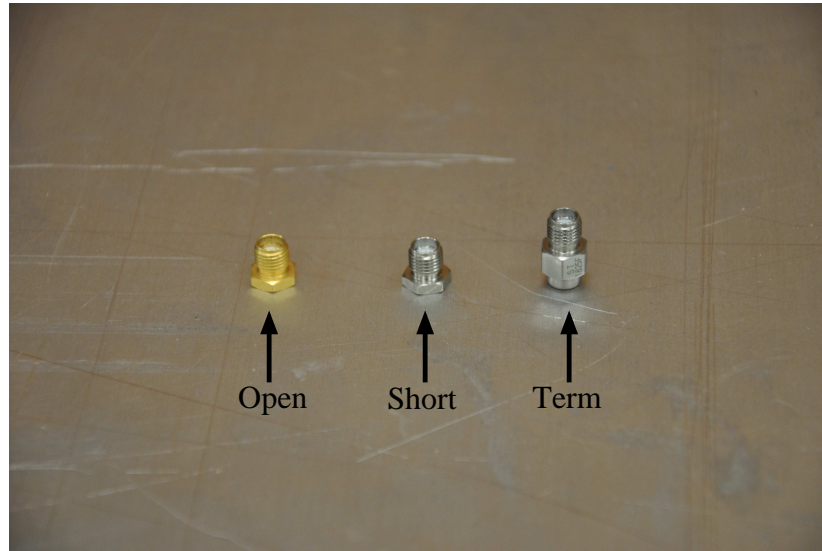
(a)
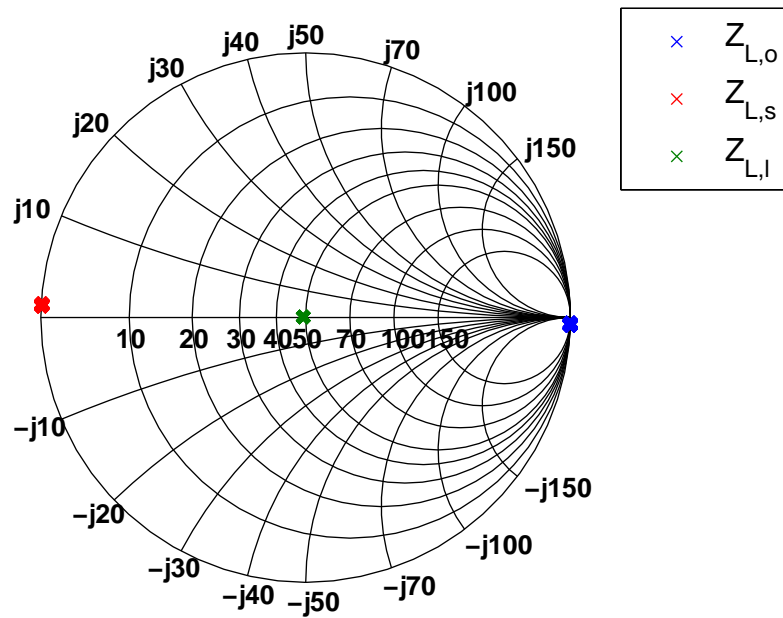
(b)

Figure 4.12. Fairview Microwave calibration standards. (a) Side view of the standards. (b) Measured load values on a Smith chart over $250 - 350$ MHz.

4.3   Measurement Results

Since the load impedances are measured values, (3.4) can be used with the precise values of Z_{L1}, Z_{L2} and Z_{L3} rather than using (3.5) for ideal load values. All three load impedances as well as the retrieved Z_{AUT} using (3.4) are referenced at the SMA mating plane while the desired Z_{AUT} is at the two-wire port as indicated in Figure 4.11(c). From $Z_{AUT,SMA}$, the reference plane can be moved to the two-wire port by deembedding the effect of the connector. In terms of the two-port Z-parameters of the connector Z_{c11}, Z_{c21}, Z_{c12}, and Z_{c22} in Figure 4.11(c), the AUT impedance at the two-wire port $Z_{AUT,\text{two-wire}}$ is found from the AUT impedance at the SMA plane, $Z_{AUT,SMA}$ by using

$$Z_{AUT,\text{two-wire}} = -Z_{c22} - \frac{Z_{c12} Z_{c21}}{Z_{AUT,SMA} - Z_{c11}}. \tag{4.1}$$

The results of $Z_{AUT,\text{two-wire}}$ reported hereafter were obtained using the connector Z-parameters from HFSS simulations. An alternative, simple model of two short transmission line sections (a coax and a two-wire) in cascade has also been tested for deembedding the SMA connector. The resulting $Z_{AUT,\text{two-wire}}$ showed little difference.

In order to study the effect of separation between the monopole (TX antenna) and the spherical helix antenna (AUT), three sets of measurements were taken with three separations—$d = 25$ cm, 50 cm and 75 cm.

4.3.1   The $d = 25$ cm case

Figure 4.5 shows that the difference between the retrieved Z_{AUT} from the indirect approach and from the direct approach at $d = 25$ cm is very small. Therefore, this close separation can be used for evaluating the AUT impedance using the assumption $Z_{AUT} = Z_{22}$ around the design frequency.

Figures 4.13 - 4.14 compares the measured and simulated responses of Z_{AUT} and $|\Gamma_{AUT}|$ of the dipole with separation $d = 25$ cm. Simulation results are for the directly

excited antenna with (red dash) and without (blue solid) the SMA connector. The two sets of simulated results show that the presence of the connector doesn't affect Z_{AUT} around the design frequency. Only over a narrow bandwidth around 320 MHz, the connector modifies the impedance noticeably and a narrowband dip in the return loss appears at 335.5 MHz. In Figure 4.14, the measured Z_{AUT} (black dash-dot), referenced at the two-wire port in Figure 4.11(b), shows a good agreement with the simulated result around the dipole's resonance frequency. The return loss shows an excellent agreement with the predicted responses in 285-315 MHz. The retrieved impedance shows a smooth variation over a broader bandwidth centered at the design frequency. Outside this range, the response becomes noisy with respect to frequency and the accuracy is lost, as can be evidenced by negative values for the antenna resistance. Figure 4.13(c) as well as Table 4.3 show that the measured Q factor is close to the simulated value.

We find that the retrieved Z_{AUT} is accurate only around the resonance frequency of the AUT. From Figure 4.12(b), the three load impedances are close to the ideal short, 50 Ω and open. Hence, (3.5) may be used instead of (3.4) to inspect the elements that contribute to the accuracy of the indirect measurement. First, all three measured Z_{in} at port 1 should be accurate for different Z_L. Figure 4.15 compares the simulated and measured Z_{in} for the three measured loads, where an excellent agreement is observed in all cases. Second, considering that the ratio between differences in Z_{in} is the critical factor in (3.5), a stronger dependence of the AUT's response in Z_{in} with respect to the load impedance Z_L will result in reliable values of Z_{AUT}. Otherwise, the numerator and denominator in (3.5) will be small numbers, and the resulting Z_{AUT} will be highly sensitive to the denominator. This is well demonstrated in Figure 4.16, where the two impedances differences appearing in the division in (3.5) are compared between simulation and measurement. Even in the significantly reduced vertical axis scale, a good agreement is observed between simulation and

measurement for both the numerator and the denominator. A perfect agreement for both quantities would be needed for accurate retrieval of Z_{AUT}. For a resonant antenna such as the spherical dipole under consideration, Z_{in} will be a strong function of Z_L only around the resonance frequency of the AUT, over which range the numerator and the denominator are significantly different from zero. As the frequency is moved away from the resonance frequency of the AUT, the retrieved Z_{AUT} starts to lose accuracy as the denominator approaches zero.

	Q	$\Delta\omega_{\text{3dB}}/\omega_0(\%)$	$\Delta\omega_{\text{10dB}}/\omega_0(\%)$
Meas.	40.40	5.03	1.70
Sim.	40.70	4.93	1.63

Table 4.3. Simulated and measured Q factors and bandwidths using the indirect approach with $d = 25$ cm.

4.3.2 The $d = 50$ cm case

Figures 4.17 - 4.18 compares the measured and simulated Z_{AUT} and $|\Gamma_{\text{AUT}}|$ of the dipole with separation $d = 50$ cm, which is a half wavelength at the design frequency. Measurement results (black dash-dot) show a good agreement with simulation results (red dash) around resonance frequency. The return loss shows an excellent agreement with the predicted response in 295-307 MHz, which is slightly narrower than the reliable frequency range retrieved with $d = 25$ cm. Around the design frequency, the retrieved antenna impedance and the reflection coefficient still confirm the enhanced bandwidth, as also shown by Table 4.4.

Figure 4.19 shows the comparison between the measured and simulated Z_{in} values for different loads. The numerator and denominator in (3.5) are plotted in Figure 4.20. A good agreement is found over the whole frequency range in all cases. However, since the separation between two antennas is larger, the coupling between two antennas is weaker, which can be observed by comparing Figure 4.15 and Figure 4.19. This
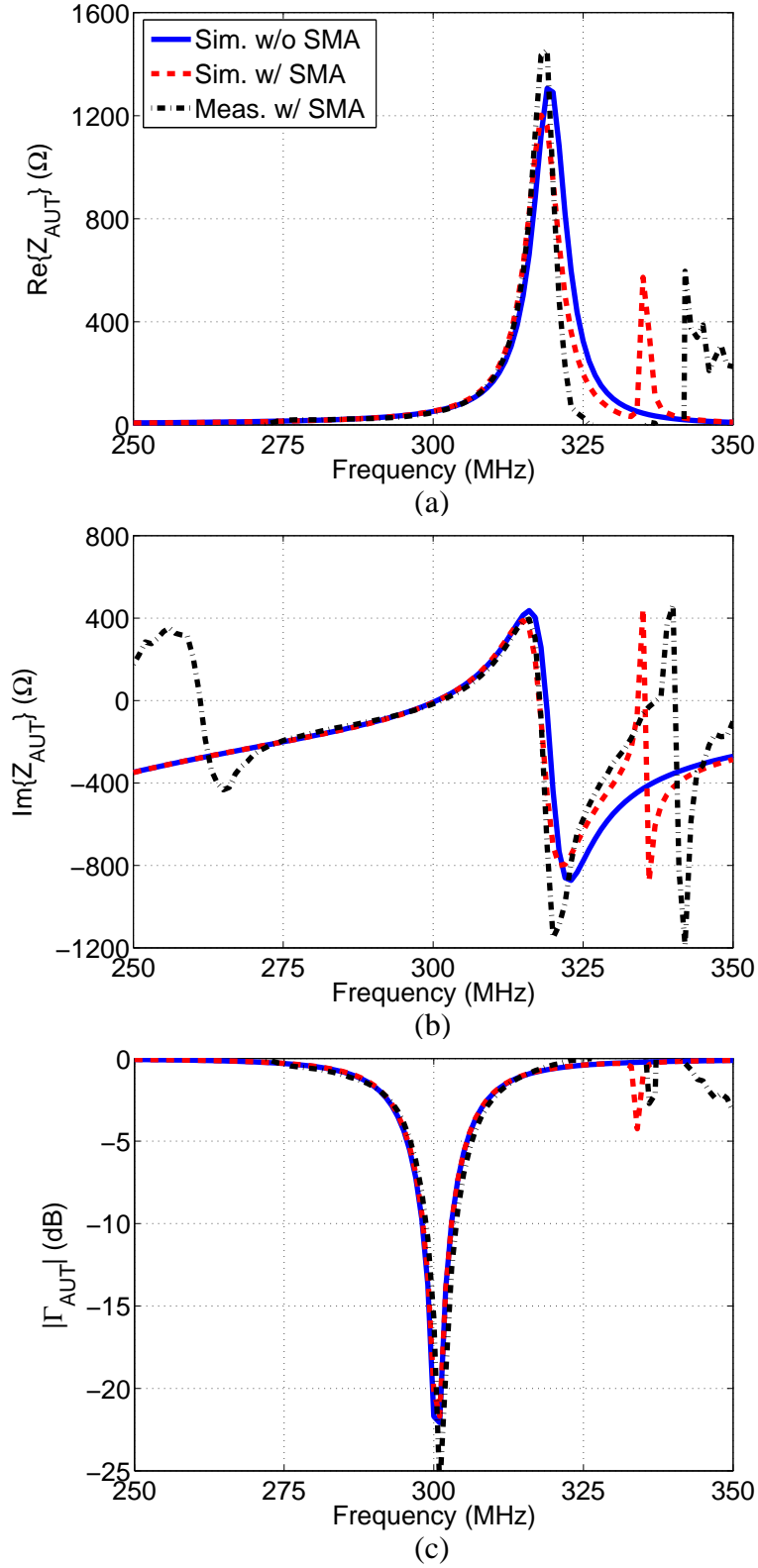
Figure 4.13. Comparison of the simulated and measured Z_{AUT} with $d = 25$ cm. (a) $\mathrm{Re}\{Z_{\mathrm{AUT}}\}$. (b) $\mathrm{Im}\{Z_{\mathrm{AUT}}\}$. (c) $|\Gamma_{\mathrm{AUT}}|$. The impedances are referenced at the two-wire port of the connector.

Figure 4.14. Comparison of the simulated and measured Z_{AUT} with $d = 25$ cm in a reduced vertical axis scale. (a) Re$\{Z_{\mathrm{AUT}}\}$. (b) Im$\{Z_{\mathrm{AUT}}\}$.
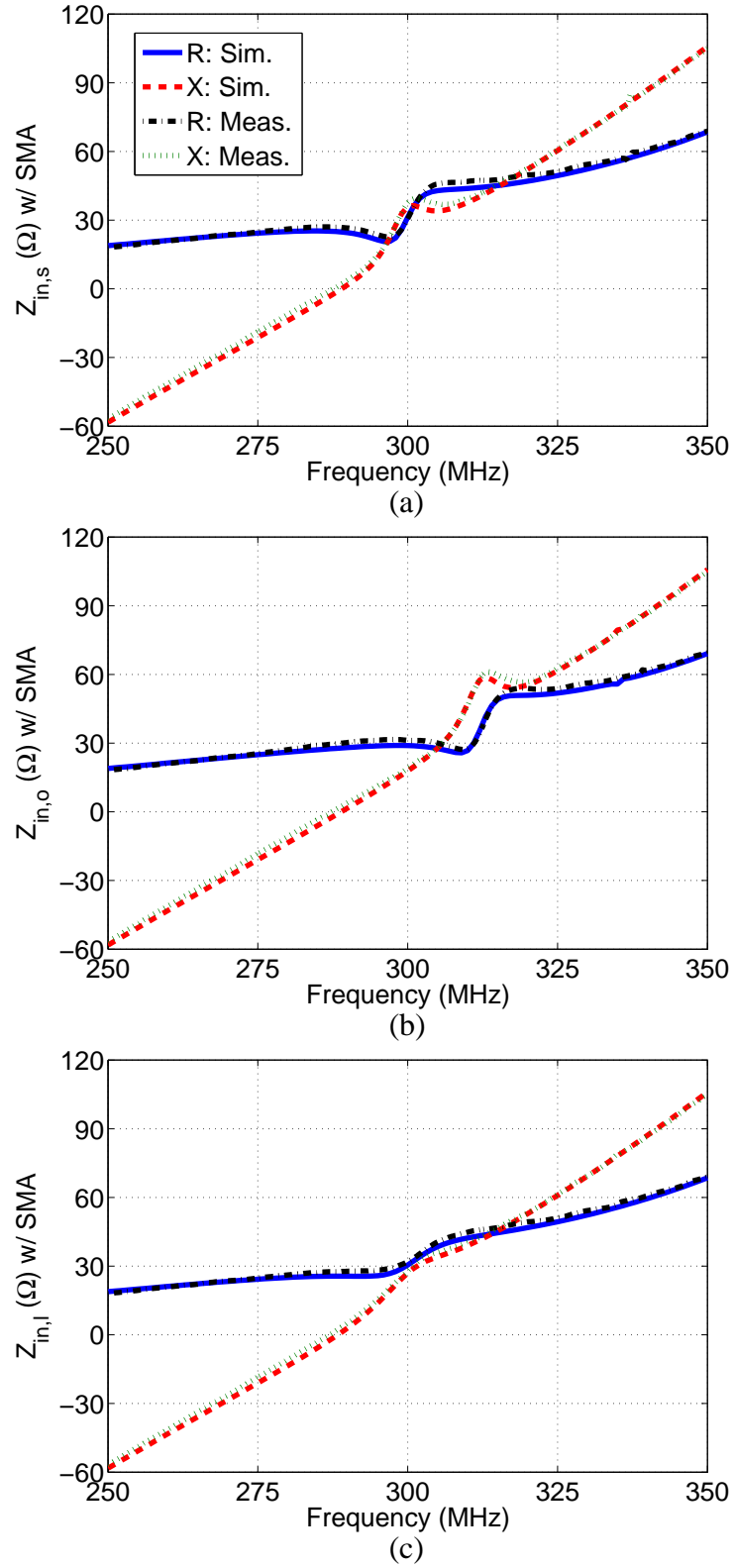
Figure 4.15. Comparison of the simulated and measured Z_{in} at port 1 with $d = 25$ cm. (a) The short standard case. (b) The open standard case. (c) The termination standard case. These impedances are referenced at the base of the monopole.
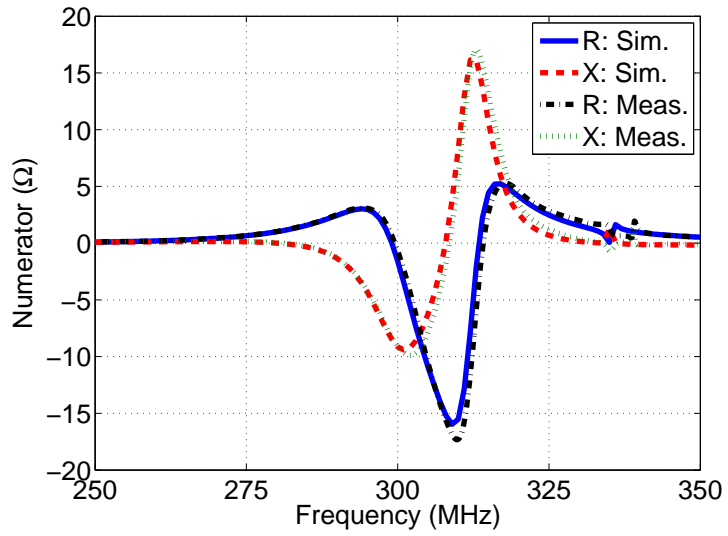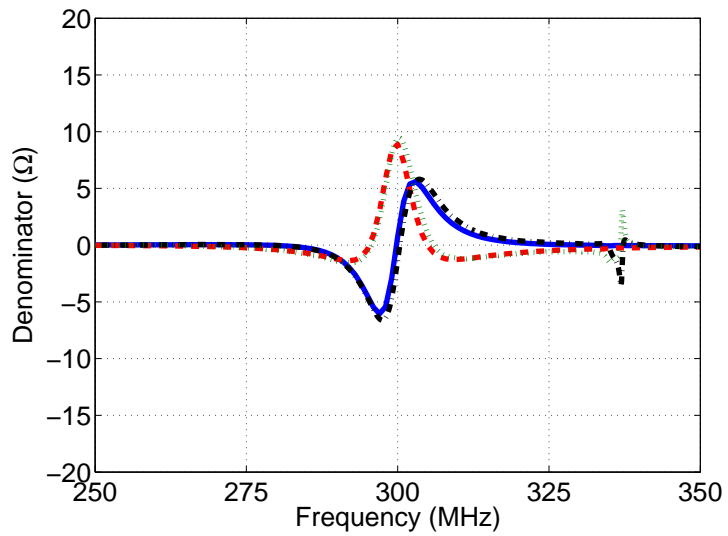
Figure 4.16. Comparison of the simulated and measured numerator and denominator in Equation (3.5) with $d = 25$ cm. (a) The numerator. (b) The denominator. They are referenced at the SMA mating plane.

weaker coupling reduces the magnitude of the impedance differences in the numerator and denominator of (3.5) as can be seen in Figure 4.20. This makes the retrieved Z_{AUT} more sensitive and hence reduce the frequency range of accurate retrieval. However, Figure 4.5 shows that, $d = 25$ cm ($0.25\ \lambda_0$) is located in a region where Z_{AUT} from the indirect approach slightly deviates from direct approach because of the structural scattering of the TX monopole. In comparison, $d = 50$ cm ($0.5\ \lambda_0$) is in the converged region, making it a better choice from the perspective of satisfying the assumption $Z_{\mathrm{AUT}} = Z_{22}$. Around the design frequency, an excellent agreement is obtained for the input reflection coefficient, verifying the enhanced bandwidth predicted by theory [7]. Both the numerator and the denominator in (3.5) being significantly different from zero (Figure 4.20) provides confidence in the retrieved $|\Gamma_{\mathrm{AUT}}|$ around 300 MHz. This is not true over the narrow range of low reflection coefficient around 260 MHz.

	Q	$\Delta\omega_{3\mathrm{dB}}/\omega_0(\%)$	$\Delta\omega_{10\mathrm{dB}}/\omega_0(\%)$
Meas.	51.57	4.47	1.47
Sim.	55.43	4.20	1.40

Table 4.4. Simulated and measured Q factors and bandwidths using the indirect approach with $d = 50$ cm.

4.3.3 The $d = 75$ cm case

Figures 4.21 - 4.24 compare the impedance and reflection coefficient quantities between simulation and measurement results. From Figure 4.21 and Figure 4.22, it can be seen that the retrieved Z_{AUT} loses accuracy even in the vicinity of the resonance frequency. Hence, even though Table 4.5 shows that the measured Q factor is close to the simulated value, it can not be concluded that the indirect measurement approach can accurately and reliably retrieve the bandwidth when $d = 75$ cm. Figure 4.23 shows a good agreement between the simulated and measured Z_{in} values at the TX antenna port with all three loads. However, due to the weak coupling between the
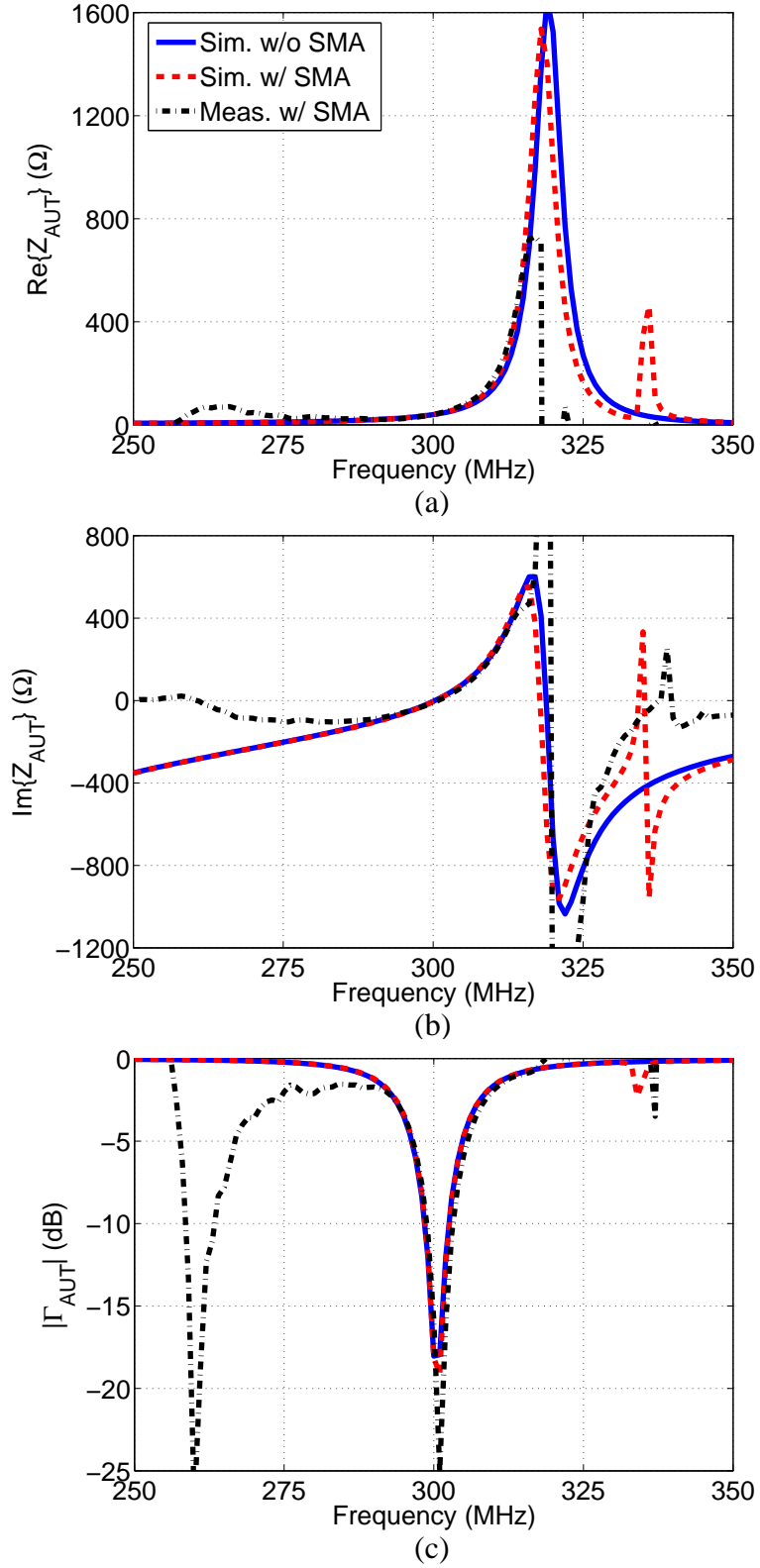
Figure 4.17. Comparison of the simulated and measured Z_{AUT} with $d = 50$ cm. (a) $\mathrm{Re}\{Z_{\mathrm{AUT}}\}$. (b) $\mathrm{Im}\{Z_{\mathrm{AUT}}\}$. (c) $|\Gamma_{\mathrm{AUT}}|$. The impedances are referenced at the two-wire port of the connector.
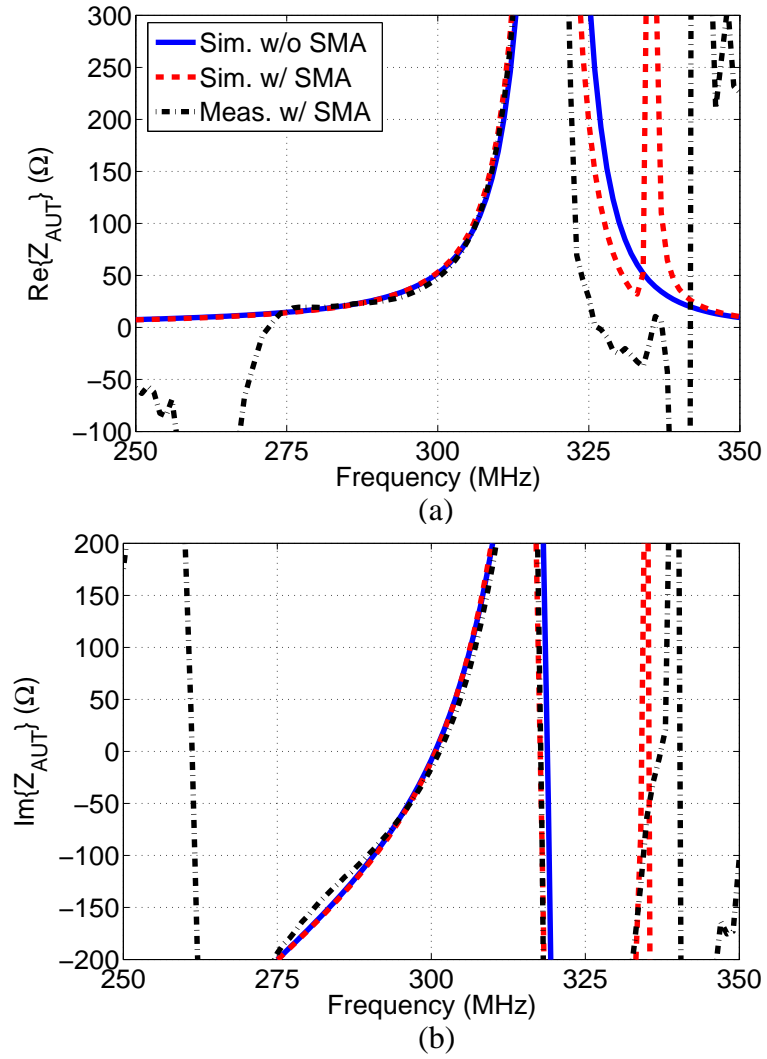
Figure 4.18. Comparison of the simulated and measured Z_{AUT} with $d = 50$ cm in a reduced vertical axis scale. (a) Re$\{Z_{\mathrm{AUT}}\}$. (b) Im$\{Z_{\mathrm{AUT}}\}$.

Figure 4.19. Comparison of the simulated and measured Z_{in} at port 1 with $d = 50$ cm. (a) The short standard case. (b) The open standard case. (c) The termination standard case. These impedances are referenced at the base of the monopole.

Figure 4.20. Comparison of the simulated and measured numerator and denominator in Equation (3.5) with $d = 50$ cm. (a) The numerator. (b) The denominator. They are referenced at the SMA mating plane.

TX antenna and the AUT, the differences among the Z_{in} values for different loads are so small that the numerator and denominator in (3.5) are closer to zero in Figure 4.24 compared with the $d = 25, 50$ cm cases shown in Figures 4.16 and 4.20. The resulting Z_{AUT} is sensitive to small variations in measured Z_{in} and becomes less accurate.

	Q	$\Delta\omega_{\text{3dB}}/\omega_0(\%)$	$\Delta\omega_{\text{10dB}}/\omega_0(\%)$
Meas.	47.26	4.97	1.60
Sim.	50.06	4.43	1.50

Table 4.5. Simulated and measured Q factors and bandwidths using the indirect approach with $d = 75$ cm.
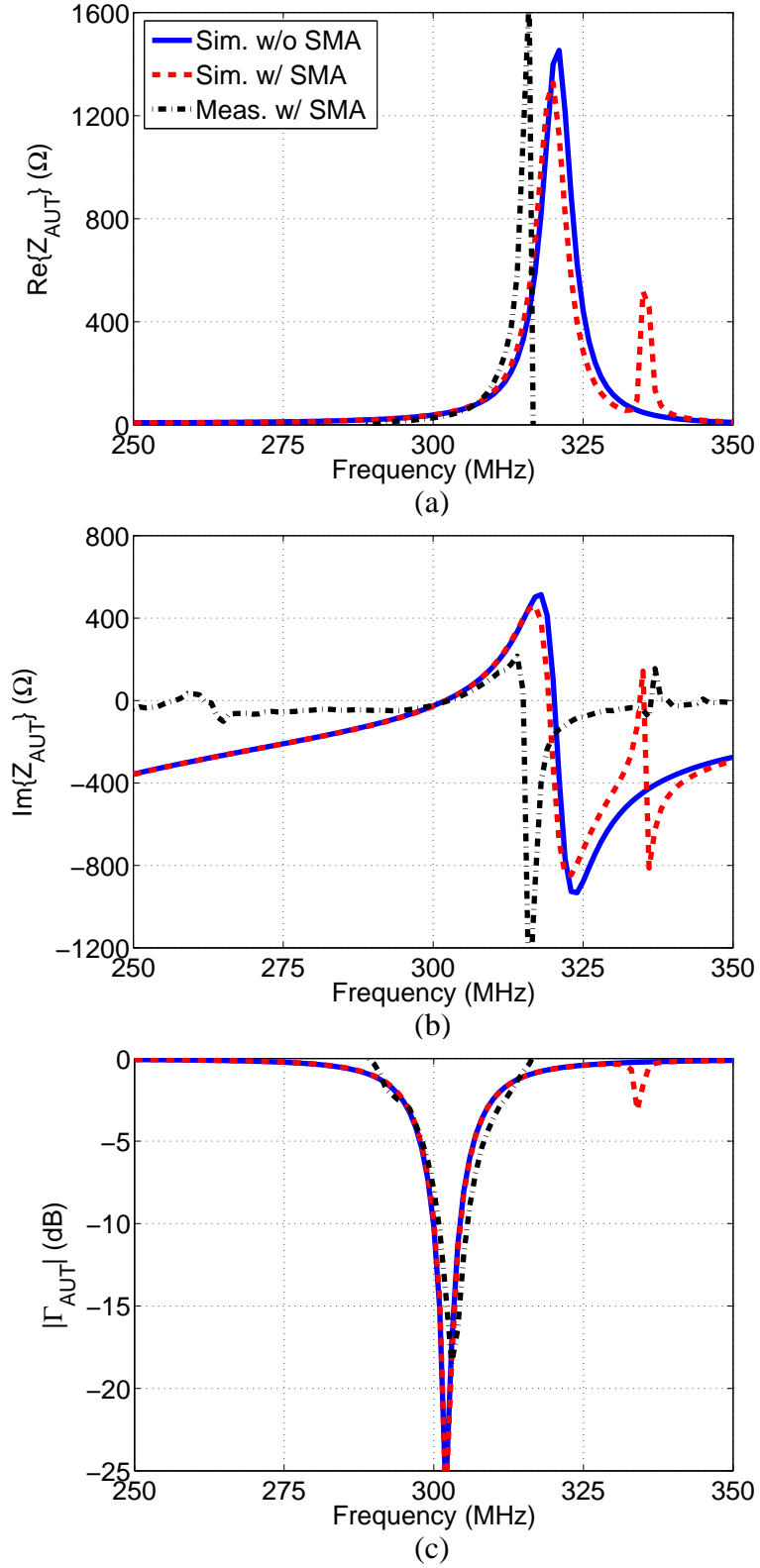
Figure 4.21. Comparison of the simulated and measured Z_{AUT} with $d = 75$ cm. (a) Re$\{Z_{\mathrm{AUT}}\}$. (b) Im$\{Z_{\mathrm{AUT}}\}$. (c) $|\Gamma_{\mathrm{AUT}}|$. The impedances are referenced at the two-wire port of the connector.
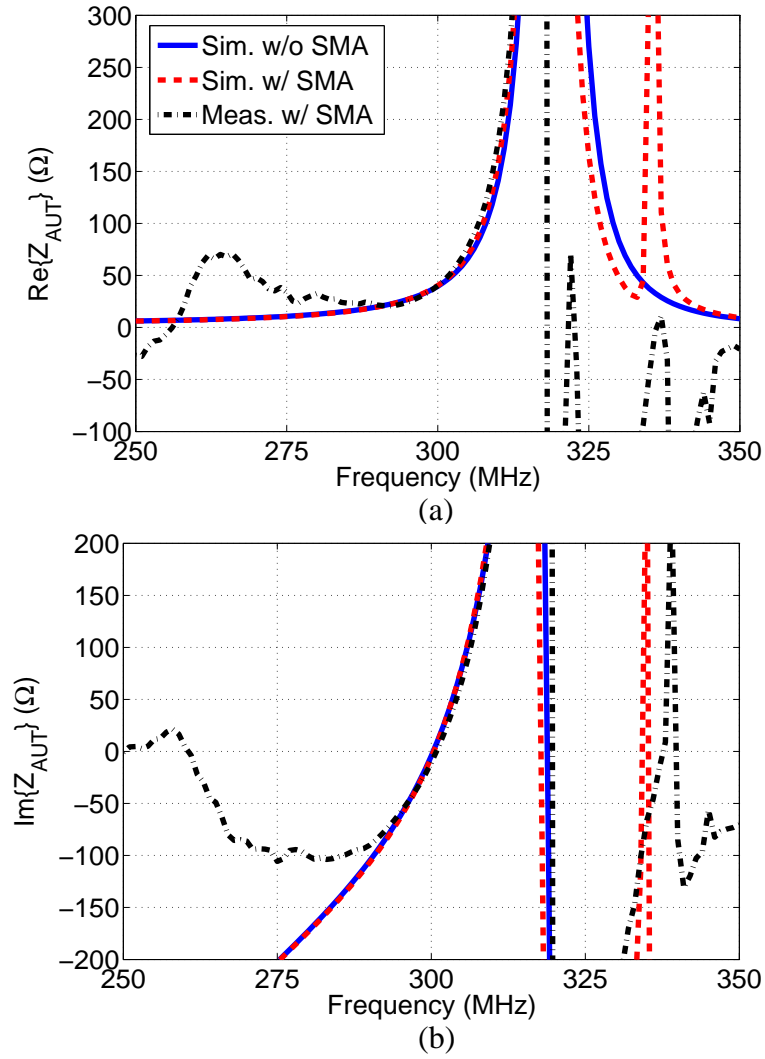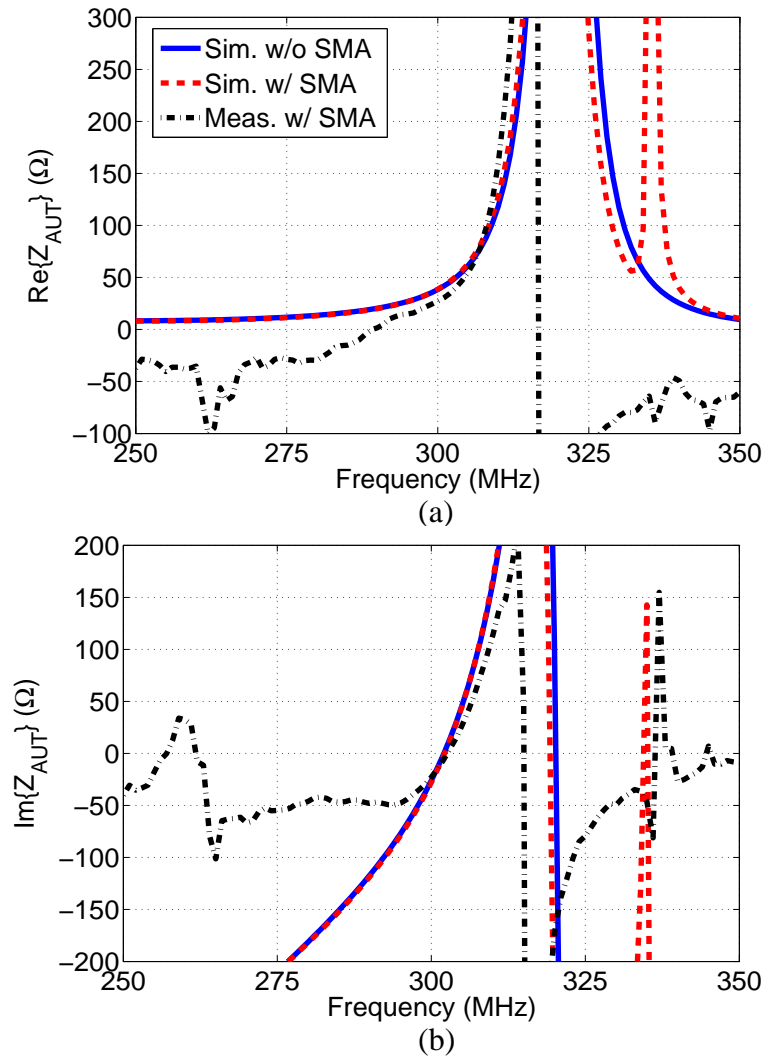
Figure 4.22. Comparison of the simulated and measured Z_{AUT} with $d = 75$ cm in a reduced vertical axis scale. (a) $\mathrm{Re}\{Z_{\mathrm{AUT}}\}$. (b) $\mathrm{Im}\{Z_{\mathrm{AUT}}\}$.
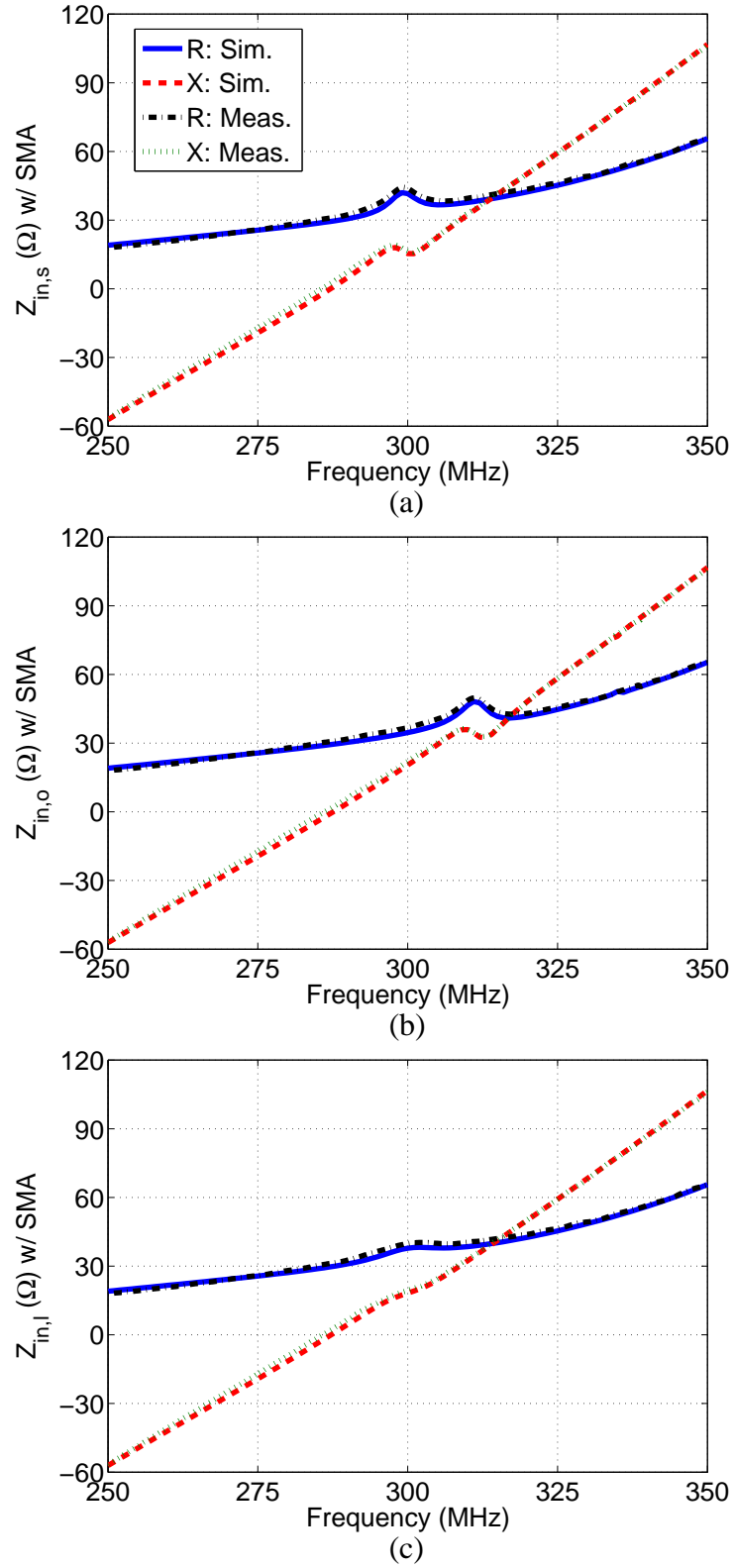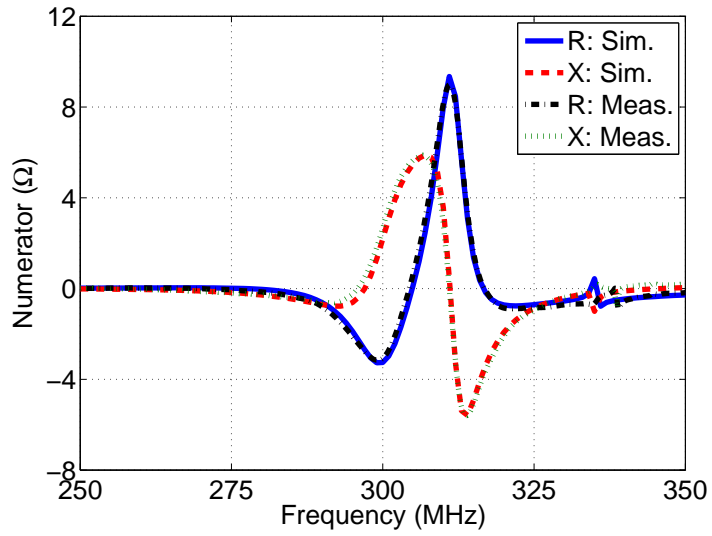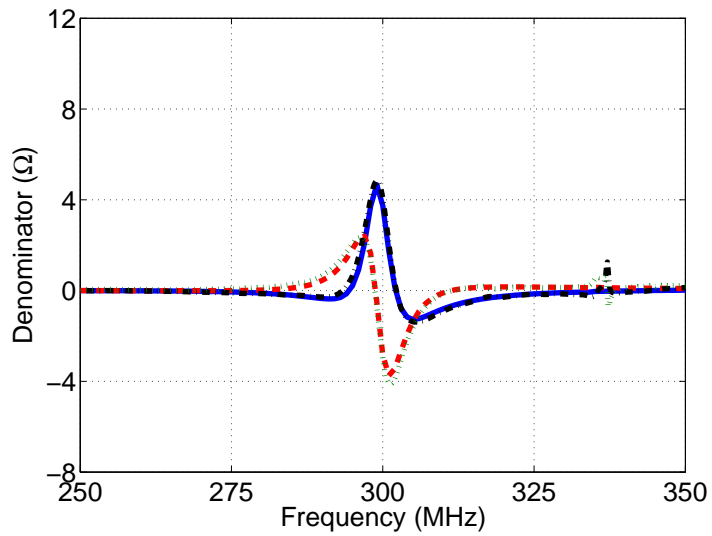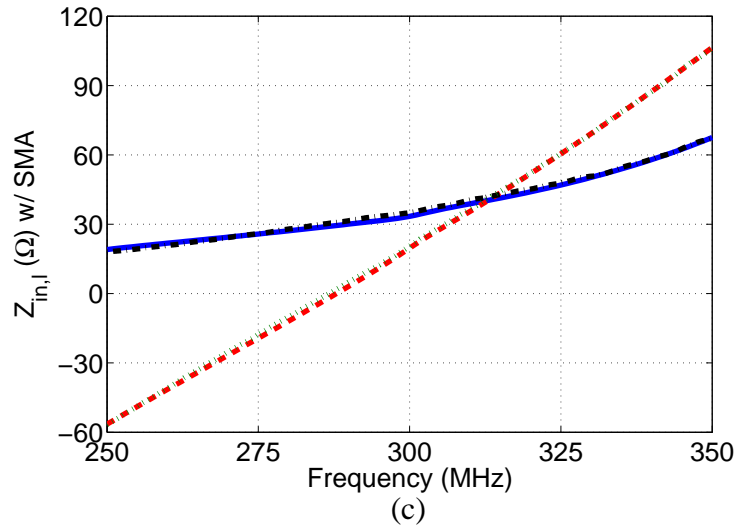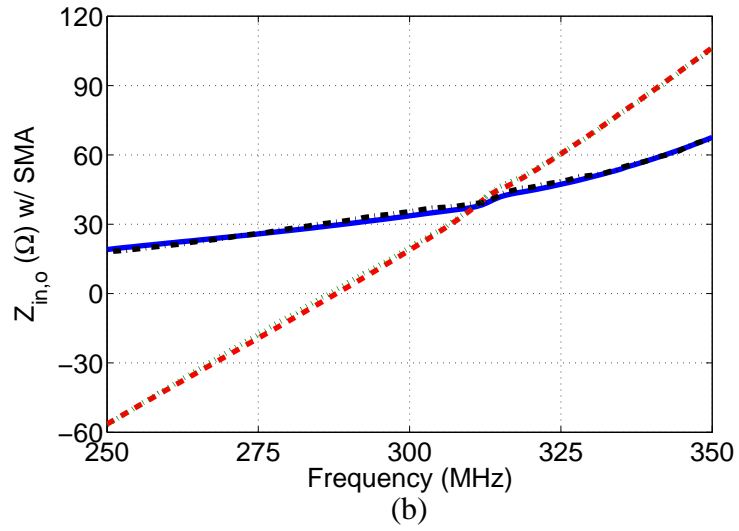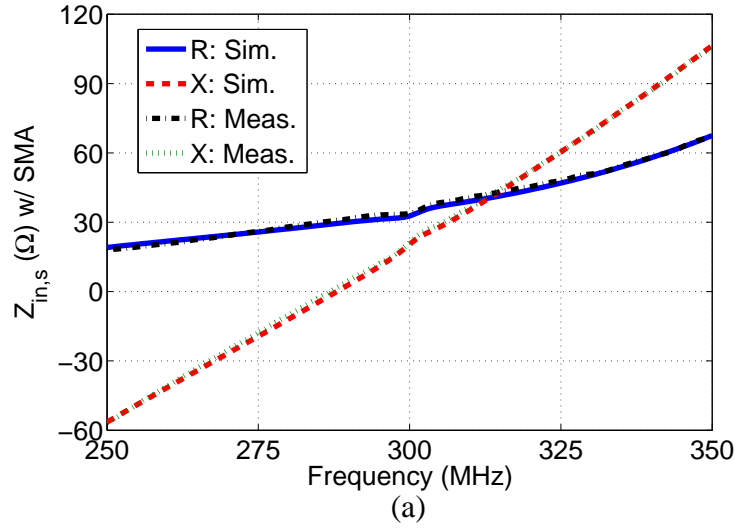
Figure 4.23. Comparison of the simulated and measured Z_{in} at port 1 with $d = 75$ cm. (a) The short standard case. (b) The open standard case. (c) The termination standard case. These impedances are referenced at the base of the monopole.
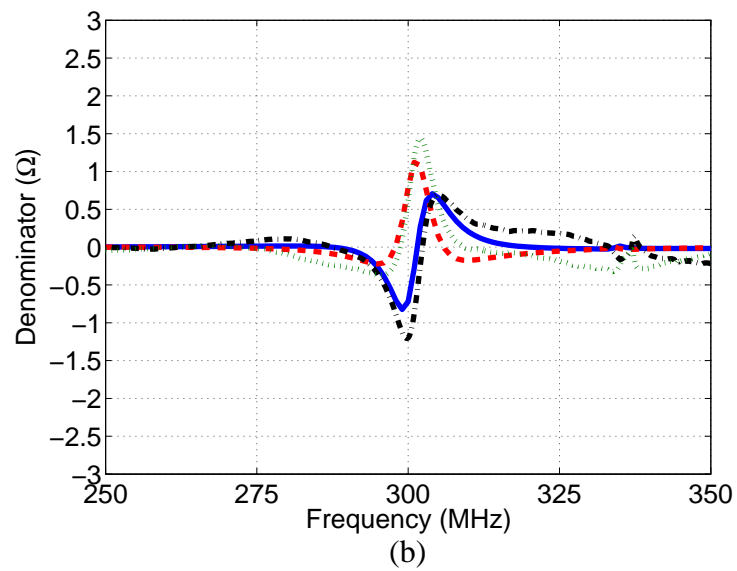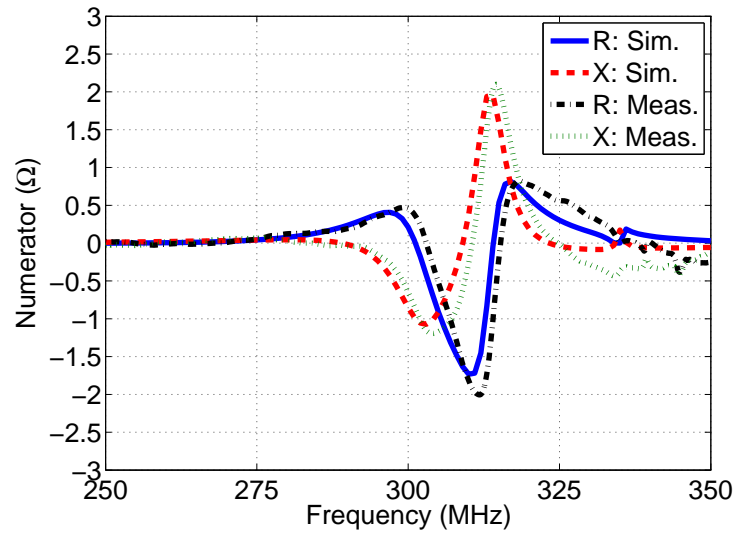
Figure 4.24. Comparison of the simulated and measured numerator and denominator in Equation (3.5) with $d = 75$ cm. (a) The numerator. (b) The denominator. They are referenced at the SMA mating plane.

CHAPTER 5

DIRECT MEASUREMENT OF A SPHERICAL DIPOLE ANTENNA OVER GROUND
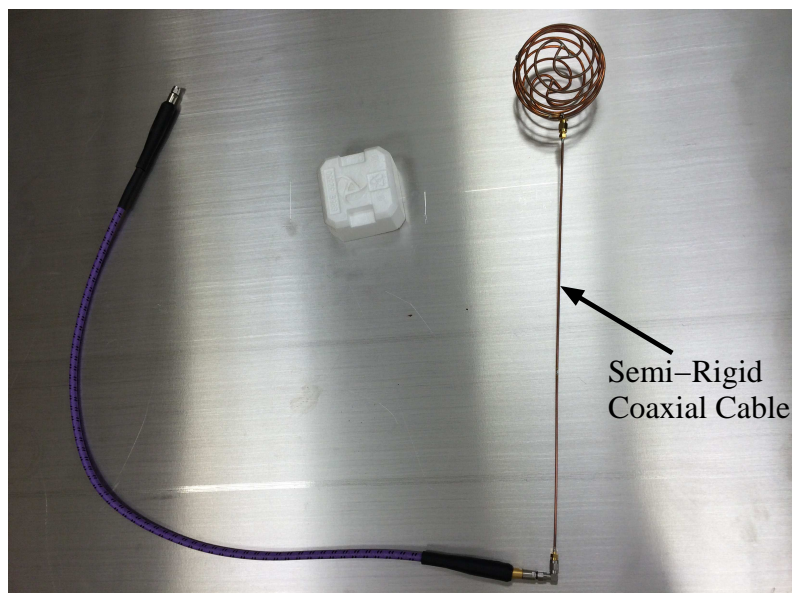
Figure 5.1. Measurement setup of spherical helix dipole antenna with direct approach.

For comparison with the indirect measurement approach of Chapter 4, several direct measurement of Z_{AUT} with an excitation cable connected to the AUT port are designed and performed. A straight, semi-rigid coaxial cable of length 40 cm ($0.4\,\lambda_0$) is connected to the AUT port with the cable axis perpendicular to the dipole axis, as shown in Figure 5.1. For reliable and repeatable connections, an SMA connector is left attached to the AUT. A standard short-open-load calibration is performed for a network analyzer measurement at the SMA mating plane. Then, (4.1) is used in

all the direct approaches to move the reference plane for Z_{AUT} from the SMA mating plane to the two-wire port of the connector shown in Figure 4.11(c).

5.1   Measurement with a Coaxial Excitation Cable

The AUT is connected to a semi-rigid coaxial cable as shown in Figure 5.2. Figures 5.3 - 5.4 compares the simulated (red dash) and measured (black dash-dot) impedances and the reflection coefficient after deembedding the SMA connector. A reasonable agreement can be obtained in the low frequency range and the agreement deteriorates with increasing frequency. The discrepancy is attributed to the leakage current over the excitation cable that effectively enlarges the antenna structure. Table 5.1 also shows that the difference between the measured and simulated Q factors is larger compared with the results using the indirect measurement approach. In fact, a measured bandwidth that is slightly broader than prediction is consistent with the size-bandwidth trade-off that an antenna of larger dimensions has a potential of achieving a broader bandwidth.
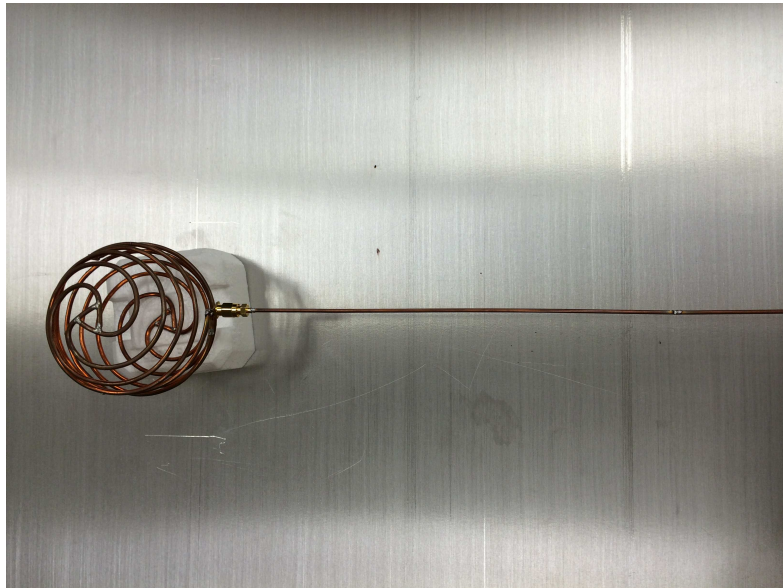
Figure 5.2. Spherical helix dipole antenna connected to a semi-rigid coaxial cable.
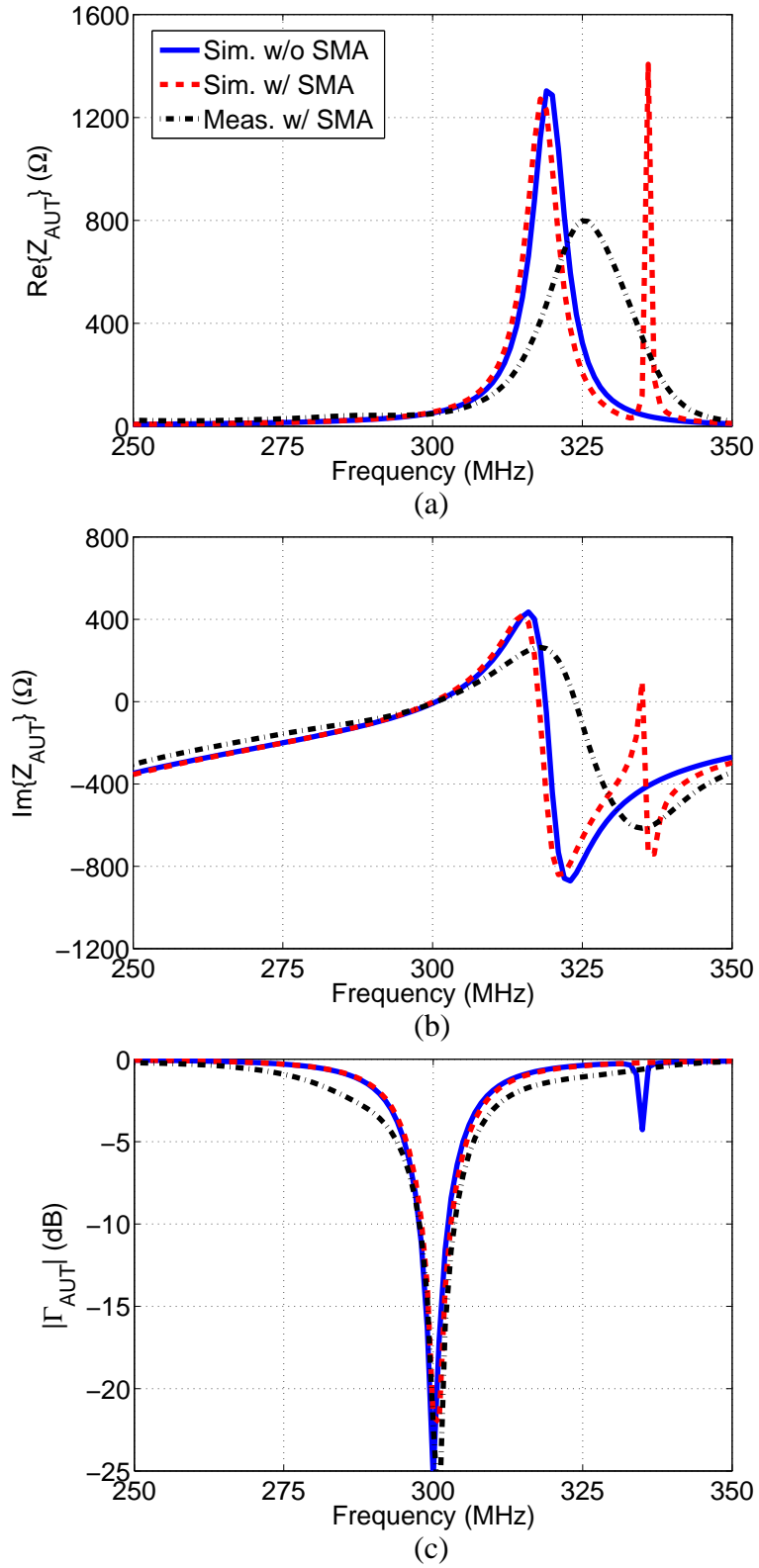
Figure 5.3. Comparison of the simulated and measured Z_{AUT} with direct excitation with semi-rigid coaxial cable. (a) $\mathrm{Re}\{Z_{\mathrm{AUT}}\}$. (b) $\mathrm{Im}\{Z_{\mathrm{AUT}}\}$. (c) $|\Gamma_{\mathrm{AUT}}|$.
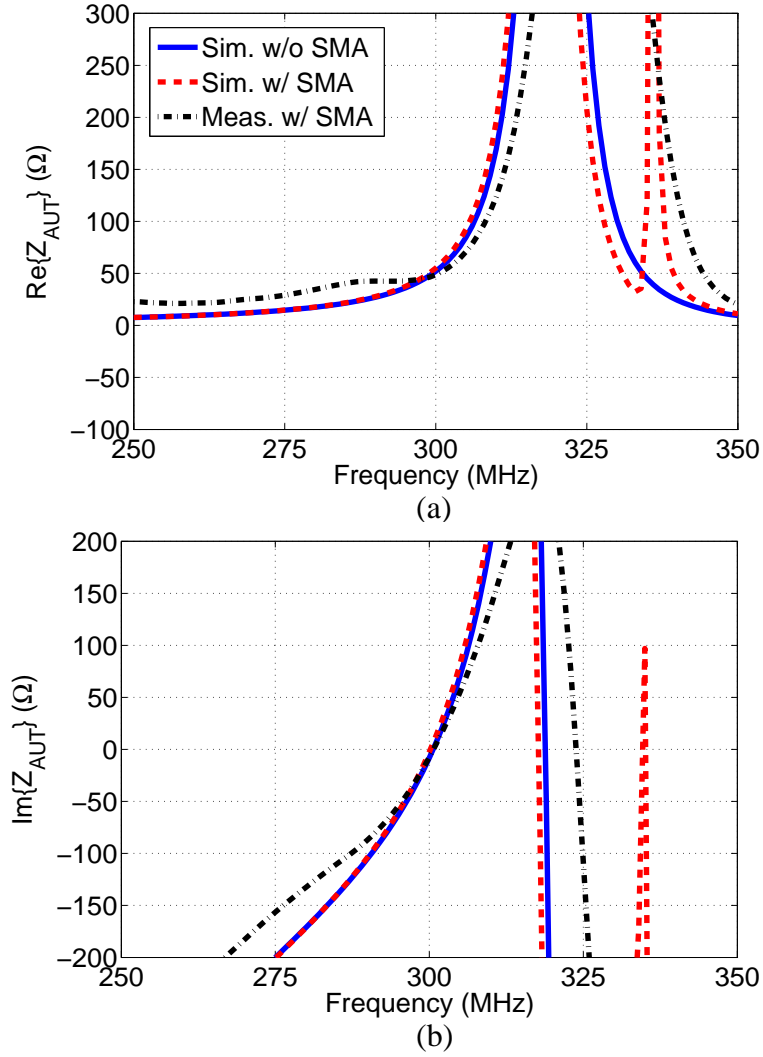
Figure 5.4. Comparison of the simulated and measured Z_{AUT} with direct excitation with semi-rigid coaxial cable in a reduced vertical axis scale. (a) $\mathrm{Re}\{Z_{\mathrm{AUT}}\}$. (b) $\mathrm{Im}\{Z_{\mathrm{AUT}}\}$.

	Q	$\Delta\omega_{\mathrm{3dB}}/\omega_0(\%)$	$\Delta\omega_{\mathrm{10dB}}/\omega_0(\%)$
Meas.	35.85	7.03	1.97
Sim.	40.62	4.83	1.63

Table 5.1. Simulated and measured Q factors and bandwidths using direct cable excitation.

5.2 Measurement with a Coaxial Excitation Cable Having Ferrite Beads

Four cylindrical-shell ferrite beads are glued to the end of the semi-rigid coaxial cable in order to mitigate cable leakage current, as shown in Figure 5.5. The ferrite beads are model HFB075024-000 from Laird Technologies.

Figures 5.6 - 5.7 show the simulated and measured result of the impedance and the input reflection coefficient of the AUT. A recognizable difference exists in the high frequency range for the measured Z_{AUT} from that of the direct excitation without ferrite beads. Otherwise, overall agreement with the simulated Z_{AUT} is similar. The measured bandwidth is slightly reduced in comparison. Table 5.2 also shows an improved Q factor result. Still, due to the direct connection of the excitation cable, it cannot be claimed that the enhanced bandwidth compared with the antenna of the same size in free space is attributed only to the presence of the ground plane.
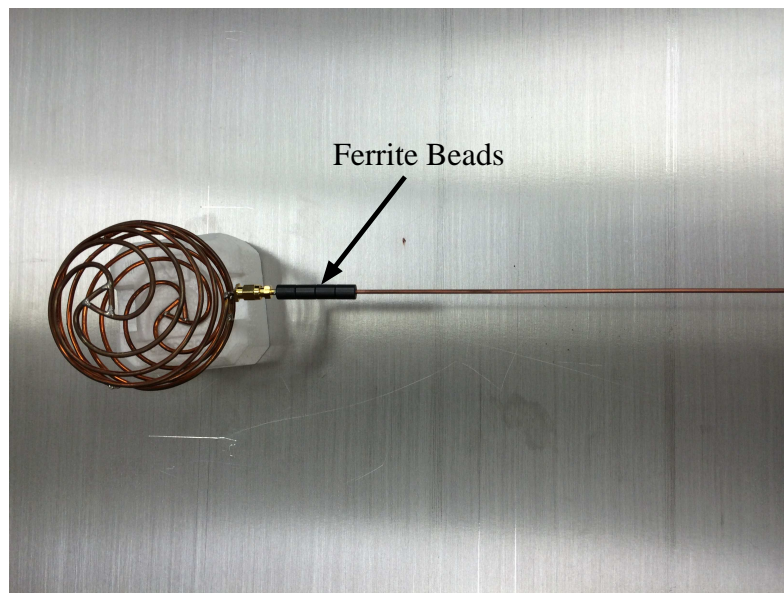
Figure 5.5. Spherical helix dipole antenna connected to a semi-rigid coaxial cable having ferrite beads.
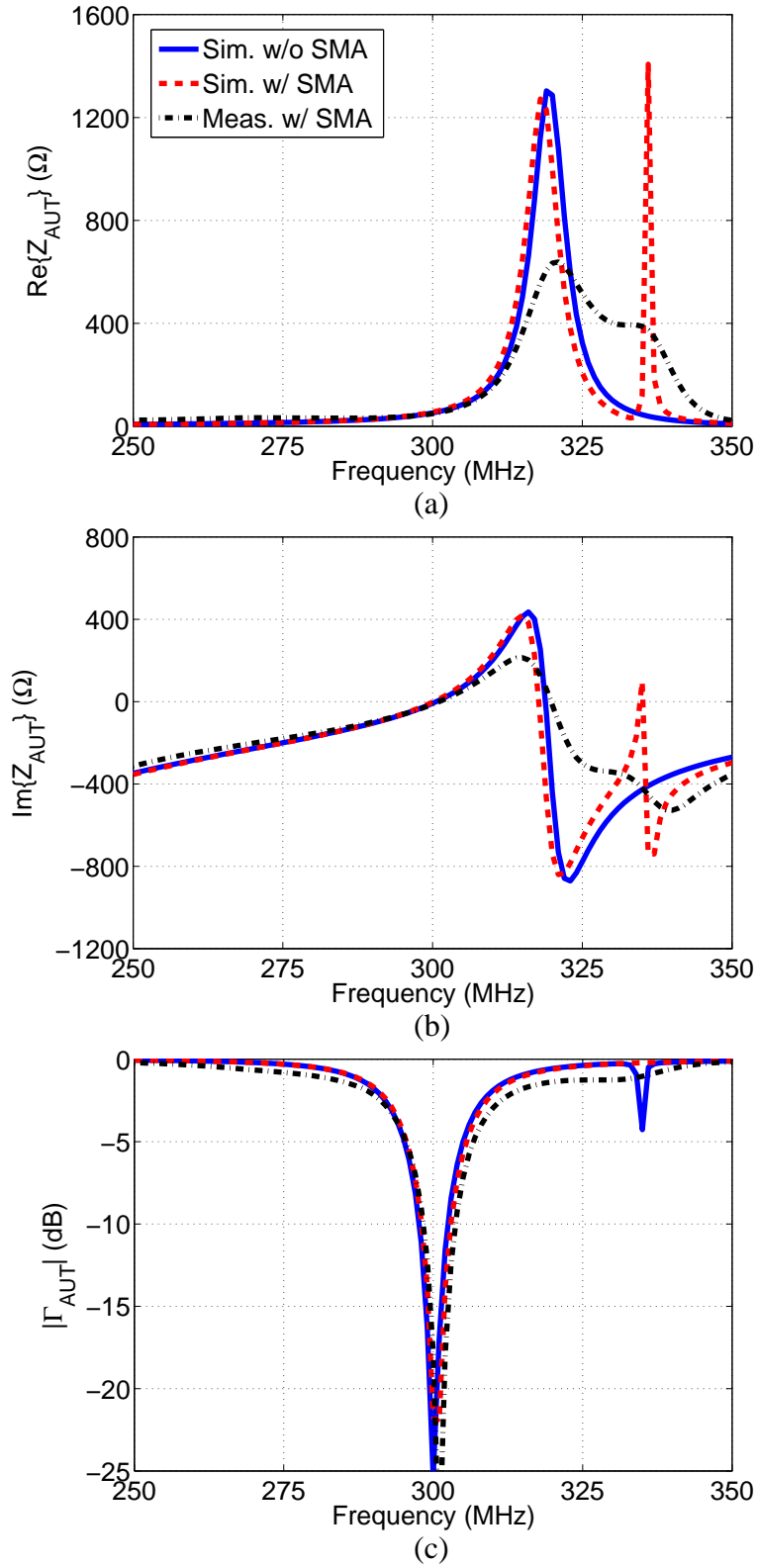
Figure 5.6. Comparison of the simulated and measured Z_{AUT} with direct excitation with semi-rigid coaxial cable having ferrite beads. (a) Re$\{Z_{\mathrm{AUT}}\}$. (b) Im$\{Z_{\mathrm{AUT}}\}$. (c) $|\Gamma_{\mathrm{AUT}}|$.
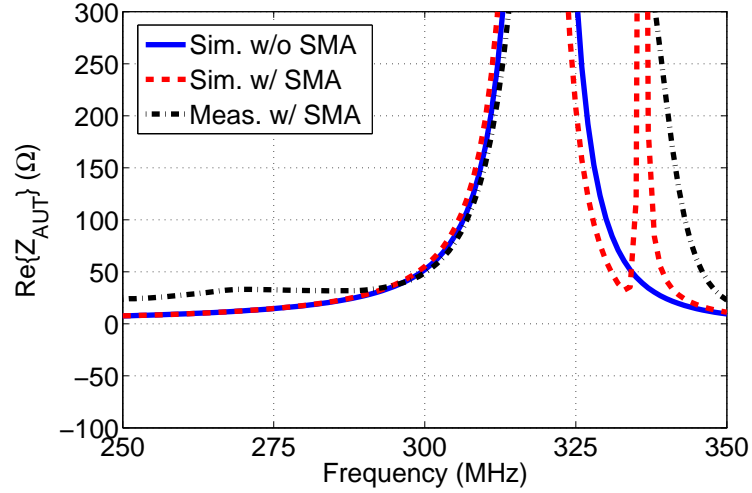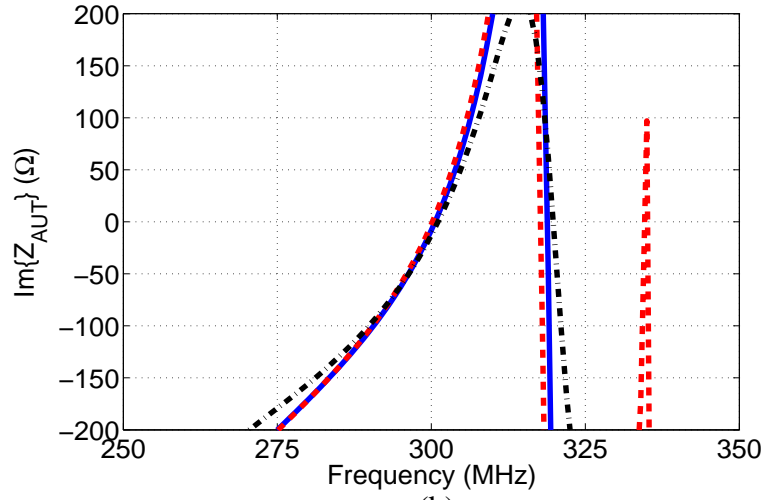
Figure 5.7. Comparison of the simulated and measured Z_{AUT} with direct excitation with semi-rigid coaxial cable having ferrite beads in a reduced vertical axis scale. (a) $\mathrm{Re}\{Z_{\mathrm{AUT}}\}$. (b) $\mathrm{Im}\{Z_{\mathrm{AUT}}\}$.

	Q	$\Delta\omega_{3\mathrm{dB}}/\omega_0(\%)$	$\Delta\omega_{10\mathrm{dB}}/\omega_0(\%)$
Meas.	37.98	5.80	1.83
Sim.	40.62	4.83	1.63

Table 5.2. Simulated and measured Q factors and bandwidths using direct cable excitation having ferrite beads.

5.3   Measurement with a Coaxial Excitation Cable with a Balun

Figure 5.8 shows a photo of the AUT connected to a semi-rigid coaxial excitation cable with a quarter-wave two-wire balun [15]. A 25 cm($\lambda_0/4$)-long copper wire is soldered to the AUT arm connected to the coax inner conductor in parallel with the semi-rigid cable and shorted together at the other end. At the connection point of the quarter-wave balun and AUT looking in, a virtual open-circuit condition can suppress cable leakage current.

Figures 5.9 - 5.10 show the simulated and measured results of the impedance and the input reflection coefficient of the AUT. An agreement better than from the previous two direct measurement methods (Figures 5.3 - 5.4 and Figures 5.6 - 5.7) between simulated and measured results are obtained. Table 5.3 also confirms this conclusion. It shows that this technique provides a better solution for suppressing cable leakage current when measuring the impedance of small antenna. However, the length of the balun is much longer than the dimension of the electrically small AUT. Since the objective of the measurement is to validate bandwidth enhancement due to the presence of a ground plane, a physically large balun attached to the small AUT still leaves uncertainty as to the underlying cause of the measured increased bandwidth.

	Q	$\Delta\omega_{3\mathrm{dB}}/\omega_0(\%)$	$\Delta\omega_{10\mathrm{dB}}/\omega_0(\%)$
Meas.	39.81	4.90	1.67
Sim.	40.62	4.83	1.63

**Table 5.3.** Simulated and measured Q factors and bandwidths using direct cable excitation having balun.
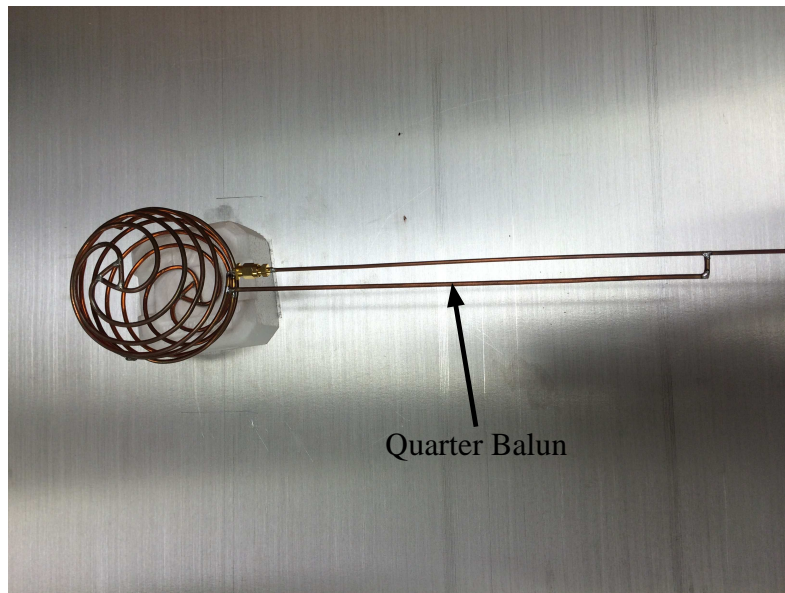
Figure 5.8. Spherical helix dipole antenna connected to a semi-rigid coaxial cable having a two-wire line balun.
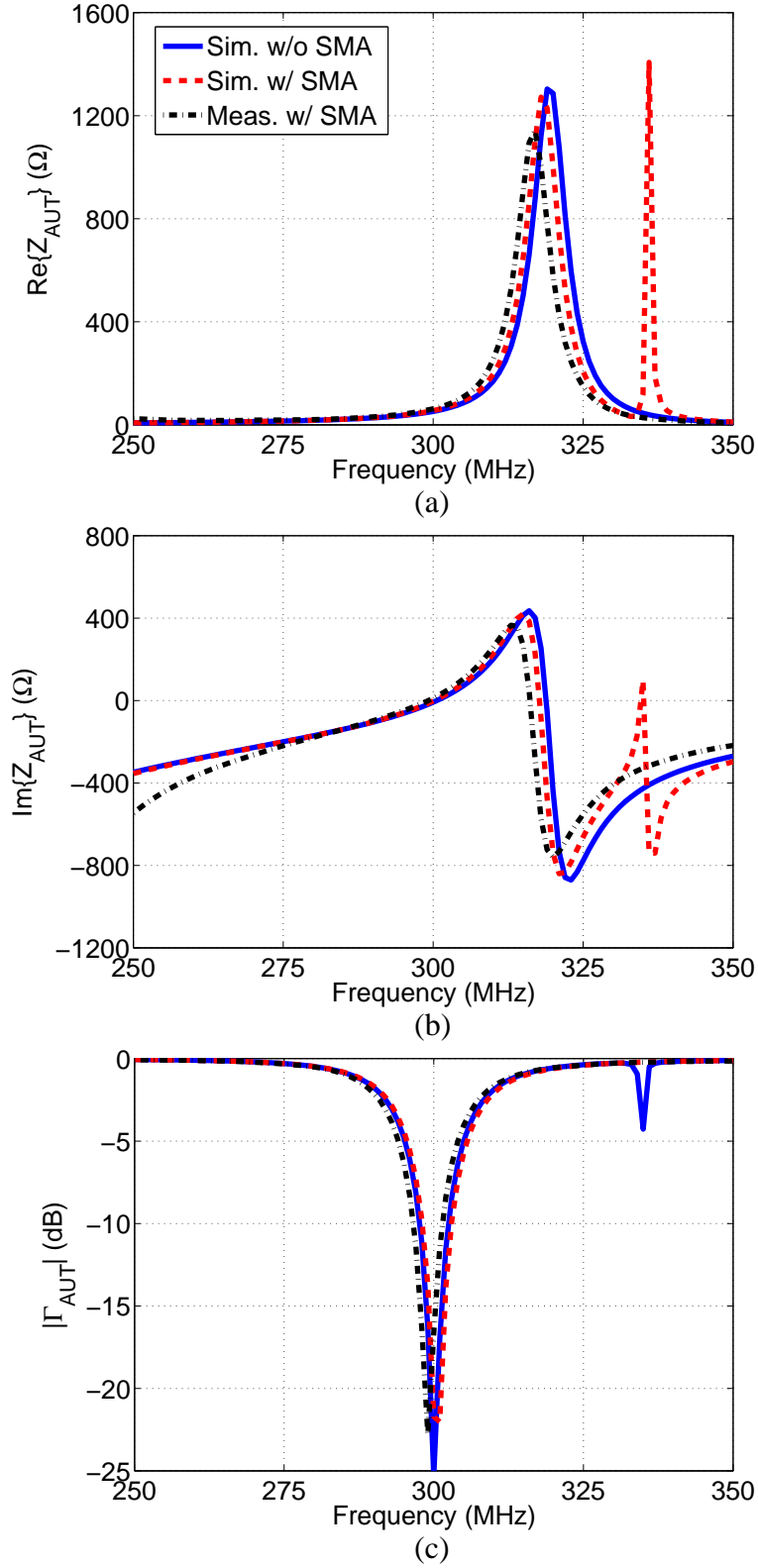
Figure 5.9. Comparison of the simulated and measured Z_{AUT} with direct excitation with semi-rigid coaxial cable and a two-wire line balun. (a) $\mathrm{Re}\{Z_{\mathrm{AUT}}\}$. (b) $\mathrm{Im}\{Z_{\mathrm{AUT}}\}$. (c) $|\Gamma_{\mathrm{AUT}}|$.

Figure 5.10. Comparison of the simulated and measured Z_{AUT} with direct excitation with semi-rigid coaxial cable and a two-wire line balun in a reduced vertical axis scale. (a) $\mathrm{Re}\{Z_{\mathrm{AUT}}\}$. (b) $\mathrm{Im}\{Z_{\mathrm{AUT}}\}$.

CHAPTER 6

CONCLUSIONS AND FUTURE WORK

6.1 Conclusions

Without direct excitation using a cable, the input impedance of a small, vertically polarized spherical helix dipole antenna over a ground plane has been indirectly measured using an interrogating antenna in a two-port network configuration. Three ca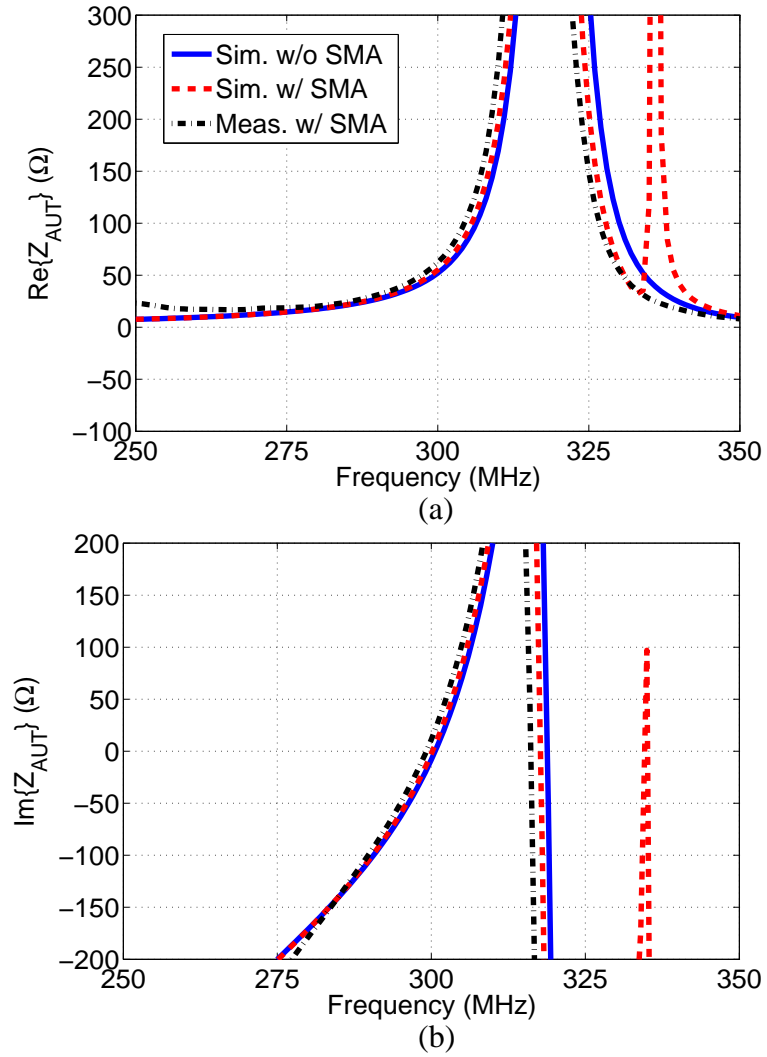libration standards with accurately measured impedances were used as loads. The impedance of the AUT was retrieved from the measured input impedances of the transmitting monopole. Measurement setup and de-embedding procedures were described for accurate retrieval of the antenna impedance. Sources of error were also discussed.

It was found that accurate impedance could be recovered even when the antennas are separated by a fraction of a wavelength. However, an analysis on the effect of the separation should be carried out first to find a suitable separation for the two-port setup, as described in Figure 4.5. The two-port network approach provides reliable impedance results around the resonance frequency of the AUT. As the separation between the two antennas increases, the retrieved impedance becomes less accurate and prone to small variations in the input impedance of the transmit antenna.

A series of impedance measurements using direct cable attachment were performed for the dipole for comparison. Although a reasonable agreement between simulated and measured impedances were found, the enhanced bandwidth results nevertheless incorporate the effect of both the ground plane and excitation cable attachment. Hence, direct measurement techniques are not appropriate for experimental validation

54

of bandwidth enhancement for vertically-polarized small antennas due to the presence of a conducting ground plane.

6.2   Future Work

Future work includes application of the two-port network approach to the impedance measurement of a small magnetic dipole over ground plane. Figure 6.1 shows a 4-arm folded slot spherical magnetic dipole antenna and it has been shown that the radiation Q of this antenna is consistent with the Thal bound for a magnetic dipole [16]. For a spherical magnetic dipole having a horizontally oriented dipole axis, the bandwidth is expected to increase when it is placed over a PEC ground plane [7]. Since a magnetic dipole antenna can not take advantage a large PEC plane as a symmetry plane, there is no monopole configuration counterpart available for accurate measurement with direct cable excitation. The indirect method in this study is applicable for accurately measuring the input impedance of the magnetic dipole antenna over a PEC ground. A magnetic loop antenna may be used as the TX antenna in the two-port network setup.

Figure 6.1. Depiction of a 4-arm folded slot spherical helix magnetic dipole [16].

BIBLIOGRAPHY

[1] K. Hirasawa and M. Haneishi, *Analysis, Design, and Measurement of Small and Low-Profile Antennas.* Boston, MA: Artech House, 1992.

[2] R. J. Garbacz, "Determination of antenna parameters by scattering cross-section measurements," *Proc. IEE*, vol. 111, no. 10, pp. 1679–1686, Oct. 1964.

[3] W. Wiesbeck and E. Heidrich, "Wide-band multiport antenna characterization by polarimetric RCS measurements," *IEEE Trans. Antennas Propag.*, vol. 46, no. 3, pp. 341–350, Mar. 1998.

[4] R. F. Harrington, "Theory of loaded scatterers," *Proc. IEE*, vol. 111, no. 4, pp. 617–623, Apr. 1964.

[5] E. F. Knott, J. F. Shaeffer, and M. T. Tuley, *Radar Cross Section*, 2nd ed. Boston, MA: Artech House, 1993.

[6] T. Yang and W. A. Davis, "Remote measurements of input impedance and radiation-Q of handheld antennas." presented at the *URSI National Radio Science Meeting*, Ottawa, Canada, Jul. 2007.

[7] H.-C. Chang, Y. H. Cho, and D.-H. Kwon, "Radiation Q bounds for small electric dipoles over a conducting ground plane," *IEEE Trans. Antennas Propag.*, vol. 62, no. 4, pp. 2031–2040, Apr. 2014.

[8] C. A. Balanis, *Antenna Theory: Analysis and Design*, 3rd ed. Hoboken, NJ: Wiley, 2005.

[9] R. Mittra and R. J. King, "An impedance transformation method for finding the load impedance of a two-port network," *IEEE Trans. Microw. Theory Tech.*, vol. 10, no. 1, pp. 13–19, Jan. 1962.

[10] R. J. Garbacz, "The determination of antenna parameters by scattering cross-section measurements: I, Antenna impedance," Ohio State Univ. Research Found., Antenna Lab., Rep. 1223-8, Sept. 1962.

[11] D. M. Pozar, *Microwave Engineering*, 4th ed. Hoboken, NJ: Wiley, 2012.

[12] S. R. Best, "Low Q electrically small linear and elliptical polarized spherical dipole antennas," *IEEE Trans. Antennas Propag.*, vol. 53, no. 3, pp. 1047–1053, Mar. 2005.

[13] H. L. Thal, "New radiation Q limits for spherical wire antennas," *IEEE Trans. Antennas Propag.*, vol. 54, pp. 2757–2763, Oct. 2006.

[14] A. D. Yaghjian and S. R. Best, "Impedance, bandwidth, and Q of antennas," *IEEE Trans. Antennas Propag.*, vol. 53, no. 4, pp. 1298–1324, Apr. 2005.

[15] K. Hirasawa and M. Haneishi, *Analysis, Disign, and Measurement of Small and Low-Profile Antennas.* Boston, MA: Artech House, 1992.

[16] S. R. Best, "A low Q electrically small magnetic (TE mode) dipole," *IEEE Antennas Wireless Propag. Lett.*, vol. 8, pp. 572–575, 2009.